A biochar supported magnetic metal organic framework for the removal of trivalent antimony

Zhu, Guocheng; Lin, Jialin; Yuan, Qian; Wang, Xiaogfeng; Zhao, Zilong; Hursthouse, Andrew S.; Wang, Zhenghua; Li, Qingbo

Published in:
Chemosphere

DOI:
10.1016/j.chemosphere.2021.131068

Published: 30/11/2021

Document Version
Peer reviewed version

A biochar supported magnetic metal organic framework for the removal of trivalent antimony

Guocheng Zhu [a,*], Jialin Lin [a], Qian Yuan [a], Xiaogfeng Wang [c], Zilong Zhao [b], Andrew S Hursthouse [d], Zhenghua Wang [a], Qingbo Li [c]

[a] Hunan Provincial Key Laboratory of Shale Gas Resource Utilization, Hunan University of Science and Technology, Xiangtan 411201, Hunan, China

[b] Department of Civil and Environmental Engineering, The Pennsylvania State University, 225 Sackett Building, University Park, PA, 16802, United States

[c] College of Environmental Science and Engineering, Dalian Maritime University, Dalian 116026, China

[d] School of Computing, Engineering & Physical Sciences, University of the West of Scotland, Paisley PA1 2BE, UK.

ABSTRACT

Metal organic framework (MOF) nanoparticles are recognized for their effective removal of metal ions from aqueous systems. However, the application of nanoparticles in a powder form as synthesized is not practical and recovery is not easy. We prepared a recyclable magnetic MOF nanoparticle phase and used a widely available waste biomass to generate biochar to support magnetic nanoparticles applied in the treatment of aqueous antimony pollution. A mushroom waste biochar was used to support a magnetic UIO-66-2COOH (denoted as BSMU). Adsorption of trivalent antimony (Sb (III)) onto the BSMU was evaluated. The results showed that optimum conditions for preparation of the BSMU were the mass ratio of MMOF to biochar 4:1, the temperature 70 ^{0}C, the time 4 h, and the initiator 4 mM. Under such conditions, sorption capacity reached 56.49 mg/g for treatment of Sb (III) solution at 100 mg/L and pH 9.1. Alkaline conditions (such as pH 9.1) are more favorable for adsorption than acidic conditions, and coexisting ions including NO_3^-, Cl^-, SO_4^{2-}, and PO_4^{3-} had

no significant negative effect in adsorption, and with the use of low dose, higher adsorption density achieved. The adsorption followed a pseudo second order kinetics model and Freundlich isotherm model. It resulted in a higher enthalpy changes (ΔH^{θ}) and activation energy (E_a) of 97.56 and 8.772 kJ/mol, respectively, and enhanced the rate pf random contact between antimony and the BSMU, as indicated by a higher entropy change (ΔS^{θ}) up to 360 J/mol·K. As a result, it readily absorbs antimony. These adsorption properties identified in this study would provide a valuable insights into the application of nanoparticles loaded biochar from abundant biomass in environmental remediation.

Keywords: Water; antimony; adsorption; biochar; nanoparticles; MOFs

Abbreviation

Sb (III), trivalent antimony

WHO, world health organization

MOF, Metal organic frameworks

MMOF, Magnetic metal organic frameworks

BSMU, biochar supported magnetic UiO-66-2COOH

FT-IR, Fourier Transform Infrared Spectroscopy

SEM, Scanning electron microscope

XPS, X-ray photoelectron spectroscopy

XRD, X-ray diffraction

TEM, transmission electron microscope

BET, Brunauer–Emmett–Teller

1 INTRODUCTION

Antimony as a hazardous toxic element and a threat to human health, causes disease such as high blood cholesterol and low blood sugar (Hatefi R., 2013). It has been shown that trivalent antimony (Sb (III)) is more toxic up to ten times than the pentavalent antimony (Sb (V)) (Yao et al., 2020). All over the world, the drinking water standard for antimony is low with world health organization (WHO) setting the regulation standard for antimony in drinking water as 20.0 μg/L (WHO, 2011) and in the United States, antimony in drinking water shall not exceed 6.0 μg/L (United States EPA, 2018). In the European Union, drinking water quality guidance value is 5.0 μg/L (Brenner et al., 2012); the standard for drinking water quality issued by China in 2006 limits the concentration of antimony in drinking water to less than 5.0 μg/L (Xiong et al., 2020). The environmental background value for antimony in natural water is very low. The average antimony concentration in world rivers has been reported 1 μg/L (Wang et al., 2011). In some regions, surface water contains a higher background value, as reported median 2.1 μg/L, compared to the median of 0.6 μg/L in groundwater (Alderton D., 2014). Where mining activities exist, localized antimony-contaminated water is produced with antimony concentration is up to 53.6 ± 46.7 μg/L (Fu et al., 2010), and has been reported to reach 9,300 μg/L (Hiller et al., 2012) in groundwater and 239 mg/L (Ritchie et al., 2013) in rivers draining mining areas, with impacts on basin sediments also severe, with antimony concentrations up to 39.0 mg/kg (B. Gao et al., 2012) at a significant distance away from primary sources. Therefore, finding a cost-effective technology for remediation of antimony pollution across diverse geographical locations is still a requirement to move towards zero pollution from current and past industrial activities.

Adsorption is the most commonly used method for treatment of hazardous substances (Huong et al., 2020; Lin et al., 2020; Guila-Almanza et al., 2021). Many solid phases have been assessed for their effectiveness in treating Sb III contamination and nanoparticles, in particular metal organic frameworks (MOF) nanoparticles show considerable promise. These are porous materials, with an adjustable pore structure, rich functional groups (Seoane et al., 2016; Fan et al., 2018; Chai et al.,

2021; Mubashir et al., 2021), and have exhibited a good sorption properties for many metal ions, such as Cr, Cu, Pd, and Sb (Vieth and Janiak, 2010), and can reach 99% removal efficiencies for metal ions including Cd^{2+}, Cr^{3+}, Pb^{2+} and Hg^{2+}. However, nanoparticles are prone to deterioration, agglomeration, oxidation and poor dispersion in liquids, thus causing a decline in their reactivity due to the influence of external factors (S.S. Cameotra and Dhanjal, 2010). Furthermore, in their synthesized powder form, application in practice is not convenient and considerable scientific research effort has been mde to provide convenient support materials. For example, O'Neill et al. (O"Neill et al., 2010) prepared a microspheric polyacrylamide as a support framework for MOF. The effectiveness of the supporting role of biochar as nanoparticles in enhancing their stability and chemical function has been demonstrated successfully. For example, Fazal et al. (Fazal et al., 2019) enhanced the removal efficacy of a dye solution by more than 99% using a biochar supported TiO_2, which enhanced the individual performance of biochar and TiO_2 alone from 85.20% and 42.6%, respectively. In our earlier research on Sb (III) sorption, we prepared a chitosan supported MOF (MIL-Fe) (Xiong et al., 2020), which has strong physical stability and a good sorption capacity and uptake. However, further investigation is needed to enhance the effect at an appropriate pH and study the inhibition of sorption from competing ionic, consequently we address the optimization of biochar to support MOF nanoparticles.

Natural biomass resources or man-made products are abundant, and have been widely used or transformed into other products to solve the problem of environmental protection (Leong et al., 2014; Wang et al., 2016; Chew et al., 2017; Hernández-Cocoletzi et al., 2020; Nagarajan et al., 2020; Ssrab et al., 2020). Biochar is a porous carbon material which can be generated from a range of organic materials such as animal bones, plant roots, sawdust and wheat straw (Sohi et al., 2010). It is characterized by a high carbon content, porous nature, abundance of functional groups and low cost for production. In China, numerous types of organic by-products generated during production of mushrooms are not reused,

and are often combusted. China is the world's largest producer of edible fungi and in 2015, the annual yield of edible fungi was 34.761 million tons (Cao, 2019). By seeking alternative applications for the waste materials negative environmental impacts from combustion can be avoided and other environmental problems can be addressed. As such, this study aimed to develop MMOF nanoparticles supported by biochar for remediation of water pollution by antimony.

In this study, we used mushroom biochar to support magnetic MOF nanoparticles (denoted as MMOF) and prepared a biochar supported magnetic UiO-66-2COOH (denoted as BSMU) composite material. The preparation and adsorption characteristics of the BSMU for removal of Sb (III) were investigated, which included wider characterization of functionality and structure to enhance the performance of magnetic MOF using biochar to adsorb antimony. Our contribution being the development of a novel adsorbent and investigating the mechanism of antimony removal by a mushroom biochar carrier of MOF nanoparticles.

2 MATERIALS AND METHOD

2.1 Materials

The chemicals used in this study included ferric chloride hexahydrate ($FeCl_3.6H_2O$) purchased from Taishan Chemical Plant Co. (Taishan, China), ethylene glycol and N, N,-dimethyl formamide (DMF) from Guangdong Guanghua Polytron Technologies Inc. (Shantou, China), tetraethyl orthosilicate (TEOS), zirconium tetrachloride ($ZrCl_4$), 1, 2, 4, 5-benzenetetracarboxylic acid (BTEC) and 3-Methacryloxypropyltrimethoxysilane (MPS) from Aladdin (Shanghai, China). Chemicals (chitosan, 2, 2-azobis [2-(2-imidazolin-2-yl) propane/dihydrochloride (VA-044)) were purchased from Macklin Biochemical Company (Shanghai, China). Potassium antimony tartrate was purchased from Tianjin Fengchuan Chemical Reagent Technologies Co., Ltd (Tianjin, China). Details of other chemicals were shown in Text S1. All solutions were

prepared with LBY-20 ultrapure water (Chongqing Owen Science and Technology Co., Ltd., China). The glassware and other laboratory ware were acid-washed, rinsed thoroughly with water, and dried prior to use.

2.2 Preparation of adsorbent

The Fe_3O_4 nanoparticles (nano-Fe_3O_4) were prepared using a solvothermal reduction and magnetic MOF (UiO-66-2COOH) was prepared by using the hydrothermal method following the process developed in our laboratory(Zhu et al., 2020). Further information about the preparation of nano-Fe_3O_4 and magnetic MOF (denoted as MMOF) is provided in supporting information (see Text S2 and Text S3). The biochar was prepared by a thermal pyrolysis reactor in the laboratory (Li et al., 2019), and the raw material, mushroom by-products, was crushed before processing. A sample of 350 g of mushroom biomass was added to the reactor and the temperature increased from room temperature to 100 ºC at a rate of 7 ºC/min and maintained for 6-8 min. Subsequently, the temperature increased to 750 ºC and the reactor heating immediately stopped. The sample was cooled to room temperature in the reactor, removed, pulverized by a roller ball mill, passed through a vibrating screen, and the sample passing a 80-100 mesh was collected. The BSMU was synthesized in situ by mixing the MMOF and the biochar in the presence of low concentration initiator 2, 2-azabis (2-imidazoline) dihydrochloride, and was carried out in a constant temperature water bath under stirring at 400 rev/min. The product was washed three times with ethanol and water and vacuum dried for 12 hours at 60 ºC, to produce the final bio-char supported MMOF for characterization.

2.3 Sorption experiment

The sorption experiment was as follows: a predetermined amount of antimony solution and adsorbent was added into 50 ml vials containing antimony stock solution, ultrapure water and buffer solution. Each vial contained a total of 50 mL of

129 solution and was immediately capped before placing on a shaker platform at 150 rev/min for 24 h. Solution pH was adjusted
130 with 0.05 M NaOH and 0.05 M HCl, which was buffered at 4.0, 6.8 and 9.1 using 0.05 M and 0.025 M potassium hydrogen
131 phthalate buffer solution and 0.01 M borate buffer solution, respectively. Preliminary test showed no significant reaction
132 occurring between buffer solution and antimony. Finally, solid adsorbent was magnetically separated from the liquid and
133 filtered using a 0.45 μm membrane, analyzed for residual antimony using an AA-7000 atomic absorbance instrument
134 (Beijing East & West Analysis Instrument Co., Ltd, China) at an sorption wavelength of 217.6 nm (Fan, 2007). Sorption
135 efficiency was evaluated by measuring sorption capacity as a ratio of adsorbed antimony (mg) to added adsorbent (mg/g)
136 as well as removal efficiency (%) of adsorbed antimony (mg/L) to initial antimony (mg/L).
137
138 **2.4 Analysis method**
139 We used Fourier Transform Infrared Spectroscopy (FT-IR) recorded on a Nicolet iZ10 FT-IR Spectrophotometer (Thermo
140 Electron Co., USA) with potassium bromide (KBr) as the dispersant to examine possible chemical bonds in adsorbents and
141 scanning electron microscopy (SEM) images of the sample were obtained using a JEOL JSM-6380LV electron microscope.
142 Specific surface areas of samples were measured using nitrogen sorption isotherms through a standard Brunauer–Emmett–
143 Teller (BET) analysis (Tristar II 3020, Micromeritics Instrument Corporation, USA). X-ray photoelectron spectroscopy
144 (XPS) recorded on an ESCALAB 250 X-ray photoelectron spectrometer (Thermo-Scientific Co., Waltham, MA, USA) was
145 used to analyze the elemental species distribution. The X-ray diffraction (XRD) patterns of the samples were characterized
146 on Rigaku Ultimate IV D/max-r A X-ray diffractometer, which was operated at 40 kV and 40 mA with Cu Ka radiation.
147 Transmission electron microscope (TEM) images of the sample were obtained using 200 KeV JEM-2100F electron
148 microscope instrument (JEOL, Japan). Specific surface areas of samples were measured using nitrogen sorption isotherms
149 through a standard Brunauer–Emmett–Teller (BET) analysis (Tristar II 3020, Micromeritics Instrument Corporation, USA).

Sorption data was fitted by pseudo-first order kinetics model (see Eq. (1)) and Pseudo-second order kinetics model (see Eq. (2)), which were expressed as follows (Xiong et al., 2020):

$$q_t = q_e(1-\exp(-k_1 t)) \quad (1)$$

$$q_t = q_e - q_e / (k_2 q_e t + 1) \quad (2)$$

Where q_t (mg/g) is a sorption capacity corresponding to a specific reaction time (t, min); q_e (mg/g) is an equilibrium sorption capacity; k_1 (min^{-1}) is a pseudo first-order sorption rate constant; k_2 (g/(mg·min)) is a pseudo second-order sorption rate constant.

Sorption rate-limiting step was analyzed using the intraparticle diffusion model as follows (Asadabadi, 2021):

$$q_t = \alpha_i + k_{3i} t^{0.5} \quad (3)$$

Where q_t is sorption capacity (mg/g) corresponding to time (t, min); α_i is constant of intraparticle diffusion model; k_{3i} is sorption rate constant, $mg/g \cdot min^{-0.5}$.

Two isothermal sorption models were investigated. Langmuir model is applicable to monolayer sorption (Pehlivan and Cetin, 2009), assuming that maximum ion exchange is determined by saturation of solute molecules in monolayer on adsorbent surface but no energy conversion occur, which is expressed using following equation (Afifi et al., 2016):

$$\frac{C_e}{q_e} = \frac{1}{q_{max} K_L} + \frac{C_e}{q_{max}} \quad (4)$$

Where q_e (mg/g) is sorption capacity; q_{max} (mg/g) is the maximum sorption capacity; K_L is Langmuir equilibrium constant; C_e (mg/L) is equilibrium pollutant concentration.

The Freundlich isotherm model assumes that sorption occurs on heterogeneous sites on a multi-layer surface (Xu et al., 2011; Tan et al., 2012). Given a multi-phase sorption surface or active site, it is suitable for single-layer (chemical) or multi-layer (physical) sorption, which is expressed using following equation (Afifi et al., 2016):

$$\ln q_e = \ln K_F + \frac{\ln C_e}{n} \tag{5}$$

Where q_e (mg/g) is sorption capacity; C_e (mg/L) is equilibrium pollutant concentration; K_F and $1/n$ are constants. K_F id related to sorption capacity. The larger K_F, the more sorption capacity it is. $1/n$ expresses a strength of bonding between absorbent and pollutant. The values between 0.1 and 0.5 show that it is easy sorption. E_a is an activation energy calculated as follows (Zhu et al., 2010):

$$\ln K_2 = \ln A - \frac{E_a}{RT} \tag{6}$$

Where K_2 ($g\cdot(mg\cdot min)^{-1}$) is sorption rate constant of Pseudo-second order kinetics; T (K) is sorption temperature; E_a ($kJ\cdot mol^{-1}$) is activation energy; A is preexponential factor; R is a gas constant, $8.314 J\cdot(mol\cdot K)^{-1}$.

Thermodynamic parameter values were calculated using the following equations (DuranoLu et al., 2012; Wen et al., 2018):

$$\Delta G^{\theta} = -RT \ln K_C \tag{7}$$

$$\ln K_C = \frac{\Delta S^{\theta}}{R} - \frac{\Delta H^{\theta}}{RT} \tag{8}$$

Where ΔH^{θ}, ΔS^{θ}, ΔG^{θ} and K_c are enthalpy changes, entropy changes, Gibbs free energy changes, and thermodynamic equilibrium constant, respectively.

3 RESULTS AND DISCUSSION

3.1 Characterization of adsorbents

3.1.1 Results of SEM

Nanoparticles included nano-Fe_3O_4, MOFs and MMOF, of which surface morphology is shown in supporting information (see Fig. S1). The BET specific surface area of MOF was 41 m^2/g with pore volume of 0.03 m^3/g. A low BET specific surface area of MMOFs was 71 m^2/g with pore volume of 0.19 m^3/g. The BET specific surface area of the biochar was bound to increase from a smaller value around 11 m^2/g to larger quantity (e.g, 55 m^2/g for $R_{MMOF/Biochar}$=1:1) and the pore volume was 0.06 m^3/g. The surface morphology of nano-Fe_3O_4 nanoparticles took a spherical shape while MOFs showed an irregular shape (see Fig. S1a-b). The size of nano-Fe_3O_4 was 300-400 nm. As shown in the Fig. S1c, the surface morphology of MMOF had the shapes of MOFs and nano-Fe_3O_4, which showed the successful combination of MOFs and nano-Fe_3O_4. The MOF nanoparticles showed good stability, as shown by their shape, and did not change significantly at pH 4.0, 6.8, and 9.1 (see TEM results in supporting information in Fig. S2). The results are beneficial to the application of nanoparticles in different pH conditions. Fig. 1 shows the surface morphology of mushroom biochar and BSMU. It showed biochar as a flaky and folded surface with random sizes and shapes (see Fig. 1a). Fig. 1b-d shows the newly created biochar supported MMOF nanoparticles and shows different amounts of nanoparticles covered the surface of the biochar. The amount was dependent on $R_{MMOF/Biochar}$ value. With the increase of the $R_{MMOF/Biochar}$ value, the amount of surface covered by nanoparticles increased. For example, a lower amount was found at $R_{MMOF/Biochar}$ 1:4 as shown in Fig. 1b. Fig. 1c shows a medium amount at $R_{MMOF/Biochar}$ 1:1 and Fig. 1d shows a further increase at $R_{MMOF/Biochar}$ 4:1. This shows the appearance of the BSMU controlled by the $R_{MMOF/Biochar}$ within a constant mass.

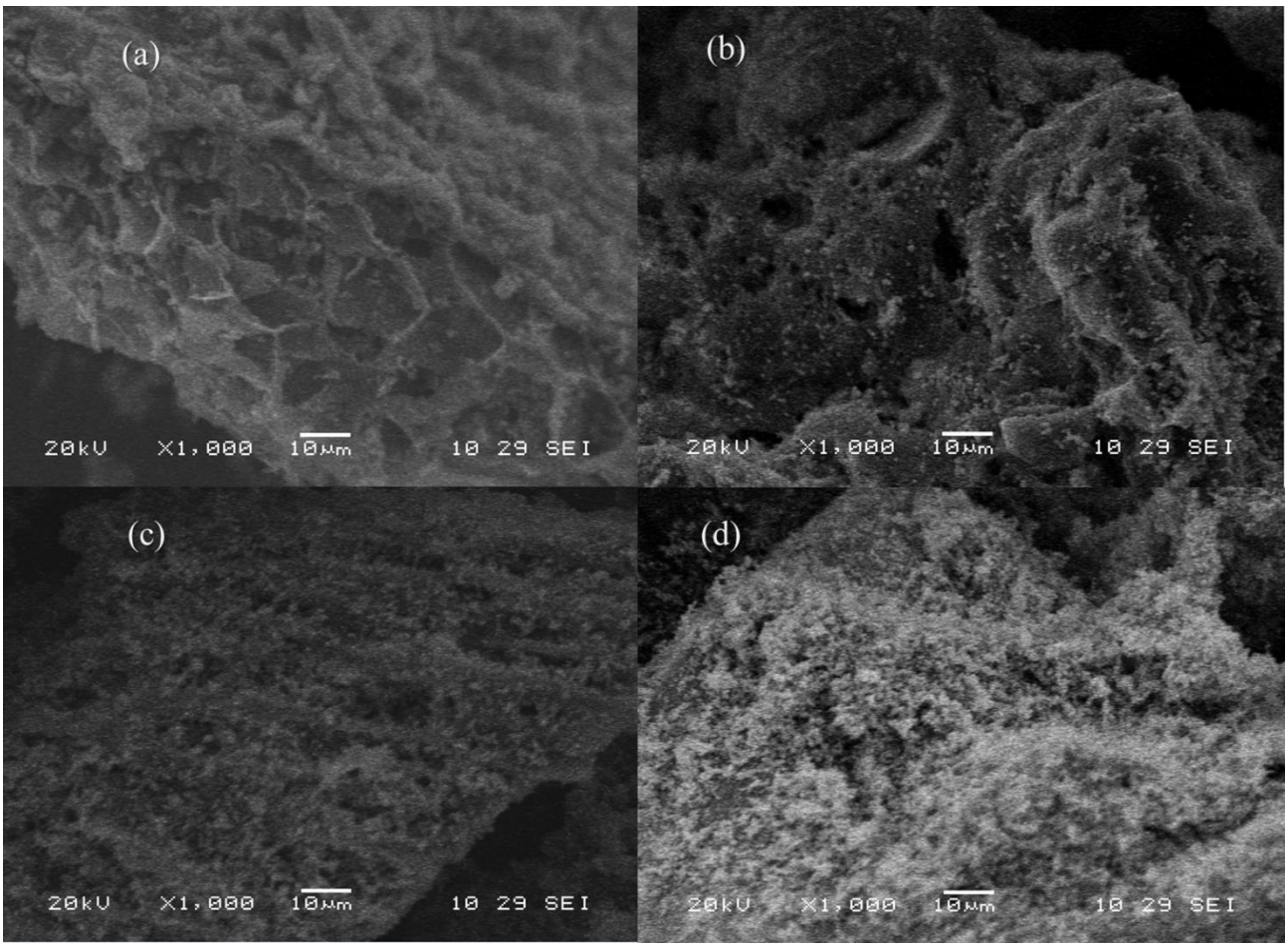

Fig. 1 SEM photographs (1000x magnification) for the virgin mushroom biochar (a), BSMU at $R_{MMOF/Biochar}$=1:4 (b), $R_{MMOF/Biochar}$=1:1 (c), and $R_{MMOF/Biochar}$=4:1 (d). The results showed that on the surface of biochar, there were numerous of nanoparticles and its amount increased with the increase of the mass ratio of $R_{MMOF/Biochar}$.

3.1.2 Results of FT-IR spectra and magnetization curves

Fourier transform infrared (FT-IR) scan of BSMU at 4000-400 cm^{-1} is shown in Fig. 2a-c. The peak characteristics corresponding to possible groups were analyzed according to infrared spectrum data (Sigma-Aldrich). In MOF, because a carboxyl group was introduced a medium O-H bending of carboxyl group appeared at 1384 cm^{-1}. The addition of an organic ligand benzene ring provided the C = C stretching peak at 1637 cm^{-1}. The biochar had a medium absorption peak at 1639 cm^{-1} which is allocated to the N-H bending vibrations of amide group (Bar et al., 2014), and at 1064 cm^{-1} a C-N stretching

peak of the amine group. When coupled with the MMOF, the N-H bending peak shifted toward low frequency vibrations at 1581 cm^{-1} and the C-N stretching vibration peak toward 1045 cm^{-1}. The peak at 1384 cm^{-1} of the BSMU resulted from original O-H bending of carboxyl group. The reason for the peak change was possibly attributed to the N-H group of biochar and carboxyl group, forming new group such as O = C–N.

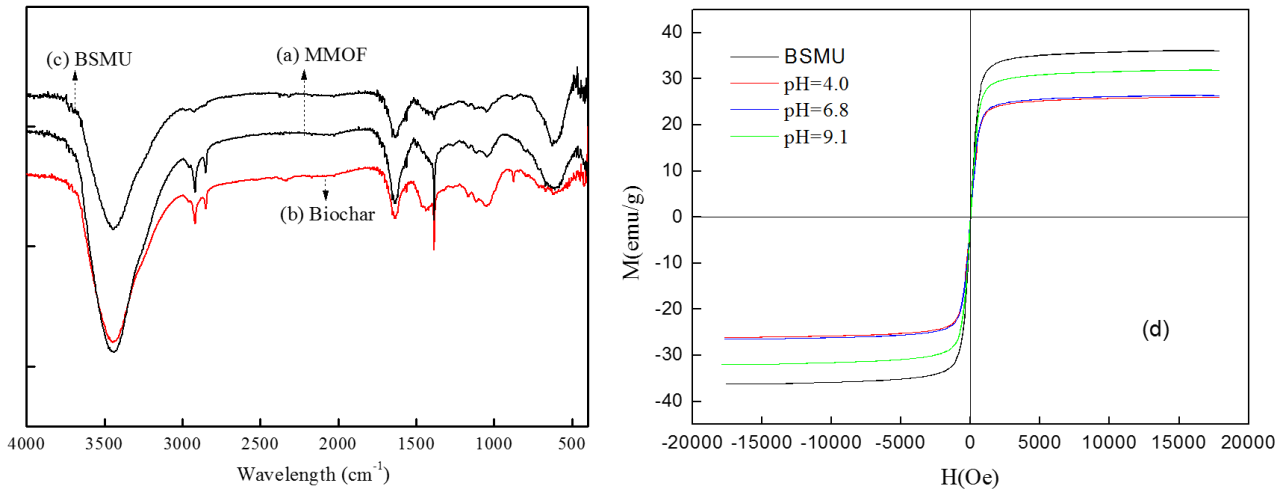

Fig. 2 FT-IR results of (a) MMOF, (b) Biochar and (c) BSMU, and the result of (d) magnetization curves

The BSMU adsorbent can be recycled and its magnetic characteristics were identified by magnetization curves as shown in Fig. 2d but they behaved differently before and after adsorption. The results showed that they were significantly affected by solution pH. The original magnetization intensity of the BSMU was 36.25 emu/g. After adsorption reaction at pH 4.0, the magnetization intensity was reduced to 26.06 emu/g, which was closer to the 26.46 emu/g at pH 6.8. At alkaline condition (pH 9.1) there was less of a reduction to a value 31.96 emu/g.

3.1.3 Results of XRD

The phase composition of the synthesized biochar, nano-Fe_3O_4, MOFs and the BSMU was confirmed with XRD analysis. Fig. 3 shows the results of their patterns. As seen from the patter of biochar shown in the Fig. 3a, the peaks at 20-30 ° are attributed to (0 0 2) of amorphous carbon (Perez and Dumont, 2020). Also, a broad hump at 2θ = 40–50° suggest the

presence of an amorphous carbon structure (Hao et al., 2021). The peaks at 2θ = 18 °, 30 °, 35 °, 43 °, 53 °, 57 °and 62 ° are attributed to (111, 220, 311, 400, 422, 511 and 440) of Fe_3O_4, which are very well matched with the standard peaks ((PDF 99–0073). As seen from Fig. 3b, the MOF had the peaks found at 2θ=7 ° (111), 8° (002), 12° (022), 14° (113), 17° (004), 22° (115), 25° (224), 33° (137) are attributed to the UIO-66 (Xie and Wan, 2019). The patterns were consistent with the report in previous literature (Zhao et al., 2016; Yang et al., 2019). The broadening of the characteristic peaks at 2θ=7°-9° showed the lower relative crystallinity. The BSMU had different XRD pattern from individual component at 2θ=10°-40° showing two broadening peaks which would be attributed to interaction active of components.

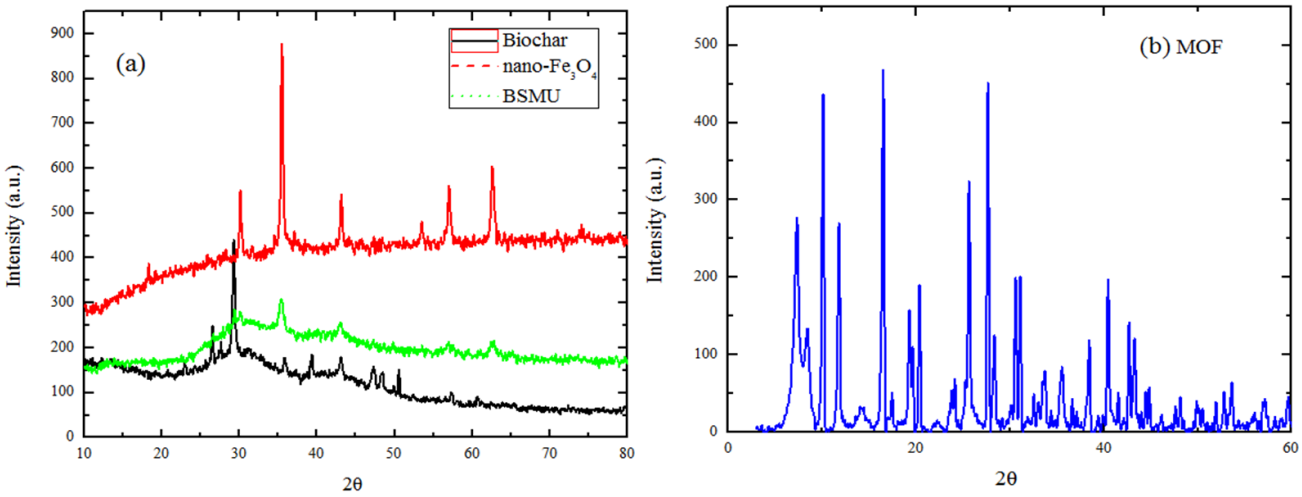

Fig. 3 XRD results of (a) nano-Fe_3O_4, biochar and BSMU, and (b) (MOF)

3.2 Effect of synthetic factors

Parameters affecting the preparation and the adsorption of antimony onto the BSMU, such as reaction temperature, reaction time, initiator concentration, and mass ratio of MMOF nanoparticles to biochar (denoted as $R_{MMOF/Biochar}$) were investigated. The influence of these parameters was evaluated by measuring sorption density (mg/g) and Sb (III) removal efficiency (%) for treatment of Sb (III) solution at 20 mg/L. The results are shown in Fig. 4.

With stirring time 2 h, initiator concentration 2 mM /L, temperature 60 °C, the effect of $R_{MMOF/Biochar}$ from 1:1 to 4:1 was

investigated. The result is shown in Fig. 4a. Low $R_{MMOF/Biochar}$ value decreased sorption density: at $R_{MMOF/Biochar}$ 1:4, the sorption density was the lowest; at $R_{MMOF/Biochar}$ 4:1, it reached the maximum removal efficiency and sorption capacity, 91 % and 9.1 mg/g, respectively. Obviously, the increased MMOF could increase the adsorption efficiency. However, to simply use more MMOF would result in a higher overall cost in application, thus in this study, we selected the ratio ($R_{MMOF/Biochar}$=4:1) as the target parameter.

For a chemical reaction, the temperature and reaction time are all important factors to ensure a sufficient reaction. As illustrated in Fig. 4b-c, At $R_{MMOF/Biochar}$ 4:1, in the range of 30 ºC to 80 ºC, an appropriate temperature was needed to reach good sorption: Low temperature such as 30 ºC was not beneficial to sorption possibly due to the insufficient reaction, resulting in an 84% removal efficiency; Increasing temperature to 70 ºC, the removal efficiency was up to 92% and sorption capacity to 9.3 mg/g but a further increase did not result in a better sorption effect. At temperature 70 ºC and $R_{MMOF/Biochar}$ 4:1, the reaction time was evaluated over a 0.5 h to 8 h period. With the increase of reaction time from 0.5 h to 2.5 h, the removal efficiency increased and the sorption capacity was up to 9.2 mg/g at 2.5 h, but over 2.5 h, reaction time had no significant influence in the sorption. Therefore, temperature 70 ºC and reaction time 2.5 h were selected as the optimum conditions for preparation of the BSMU.

Initiator is often added to the system to prepare MOF or MOF nanoparticles loaded organic monomer in order to initiate copolymerization, possibly enhancing stabilization of the nanoparticles (Bo Wang, 2016; Yunchun Liu, 2018; Linbing Sun, 2019; Zhenyu Lou, 2021). As seen from our investigation, initiator had a good effect on the stabilization of the MMOF loaded biochar by examining its appearance and adsorption performance. As shown in the photo of Fig. S3 in the supporting information without the initiator, the adsorbent is a heterogeneous mixture. The initiator enhanced the dispersion and

stability of the nanoparticles on the biochar and resulted in good sorption performance. In detail, the effect of initiator concentration in the range of 0 to 8 mM on sorption was investigated at $R_{MMOF/Biochar}$ 4:1, temperature 70 °C, reaction time 2.5 h. The result is shown in Fig. 4d. Obviously, it had a higher sorption density in the presence of initiator and at 4 mM the sorption capacity achieved the maximum. With the increase of the initiator concentration up to 4 mM, the removal efficiency increased to the maximum value, 93%. Further increasing initiator concentration, no notable enhancement occurred and at 8 mM there was a slight decrease. Therefore, we selected 4 mM as an optimum initiator concentration.

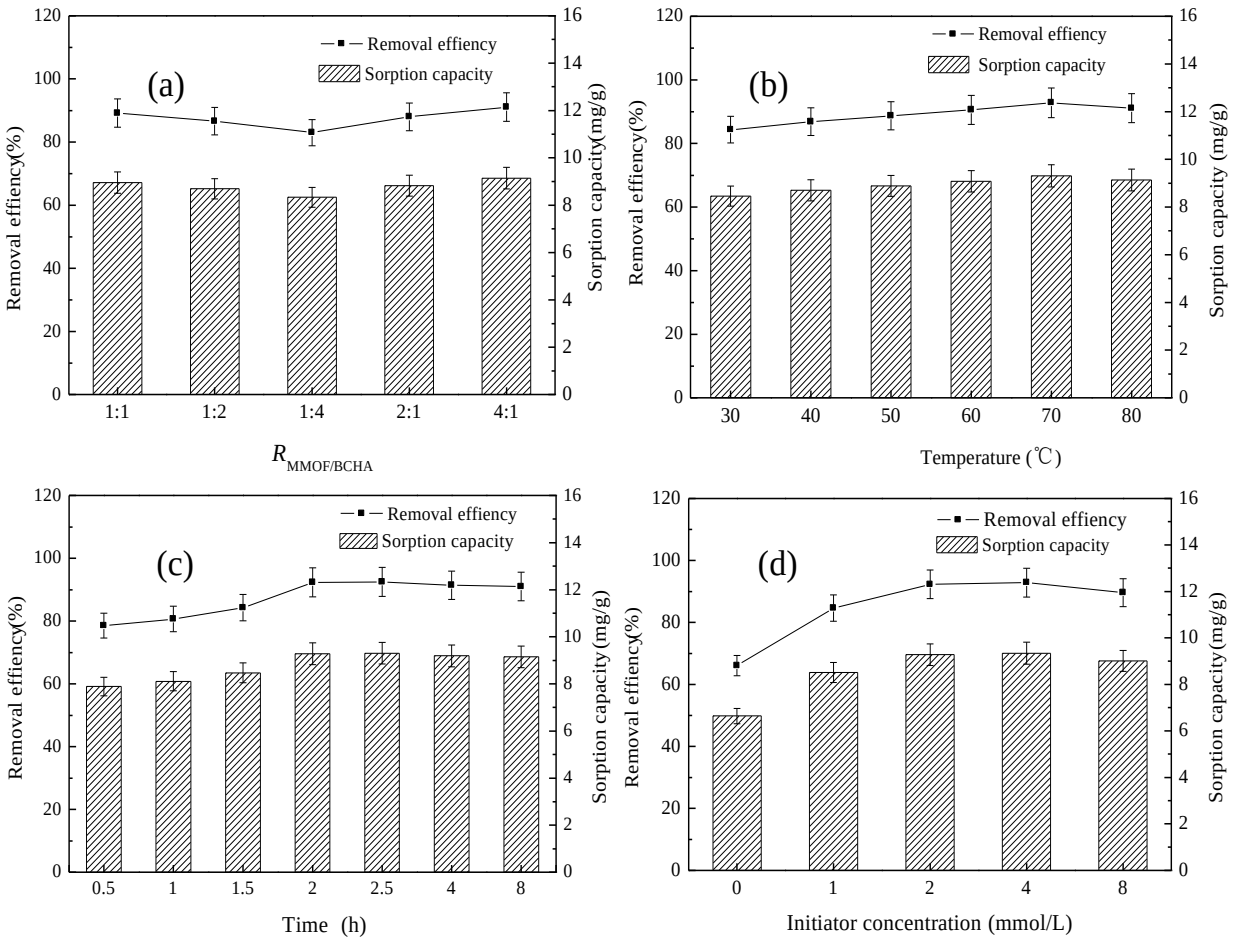

Fig. 4 Effect of preparation conditions on sorption density: (a) mass ratio of $R_{MMOF/Biochar}$, (b) temperature, (c) time, and (d) initiator concentration. The results showed that a wider range of synthetic conditions of biochar supported MMOF could be applied.

3.3 Effect of adsorbent dosage at different pH

The BSMU had a different sorption effect for antimony removal under a varying pH, which differs from sorption of antimony by other adsorbents. It has been shown previously that Sb (III) sorption is relatively insensitive to pH and is generally best in an acid environment. However, there are circumstances where suitable adsorbents can be found for acid, neutral and alkaline pH. For example, ferric hydroxide had a better sorption effect in an acidic environment (He et al., 2015). The Zirconium oxide (ZrO_2)-carbon nanofibers have best performance at pH 7.0 (Luo et al., 2015). The MIL-Fe and chitosan supported MIL-Fe metal organic materials perform best in alkaline conditions (Cheng et al., 2020; Xiong et al., 2020). However, Zirconium-based metal−organic frameworks (NU-1000) and goethite show have a negligible influence of pH on Sb (III) sorption over the range pH 2 to 11 (Li et al., 2017). Therefore, pH effect is dependent on type of adsorbent, and determining the response for the new material synthesized here is critical. It is suggested that the effect of pH is dominated by the antimony species and the electro kinetic properties of adsorbent (Ungureanu et al., 2015). The pH effect tested in this study was investigated at Sb (III) concentration 20 mg/L, pH (4.0, 6.8 and 9.1), the BSMU dose between 20 mg to 100 mg, temperature 303 K, rapid stirring 150 rev/min and sorption time of 24 h. The results are shown in Fig. 5. As illustrated in Fig. 5a-b, sorption density descended in the order pH: 9.1 > 6.8 > 4.0 for all adsorbent doses. As seen from the investigation, an alkaline condition was beneficial to sorption and an acidic condition had an inhibition effect. As expected, with the increase of the adsorbent dose, the removal efficiency of antimony increased and a low adsorbent dose resulted in a higher sorption density. The decay of adsorption capacity (q_D) with adsorbent dosage could be expressed using an exponential decay model as follows:

$$q_D = a e^{-D/k} + b \tag{9}$$

Where q_D is sorption capacity (mg/g) corresponding to a fixed adsorbent dosage; a is amplitude constant; D is adsorbent dosage; k is decay constant and b is offset value.

The parameters of exponential decay model are shown in Table S1. The fitting correlation coefficient (R^2) achieved 0.998, 0.986 and 0.986 at pH 4.0, 6.8 and 9.1, respectively. At pH 4.0, the decay constant was 57.984, which was larger than others (41.974 for pH 6.8 and 42.156 for pH 9.1). It was not conductive to the adsorption under acid condition.

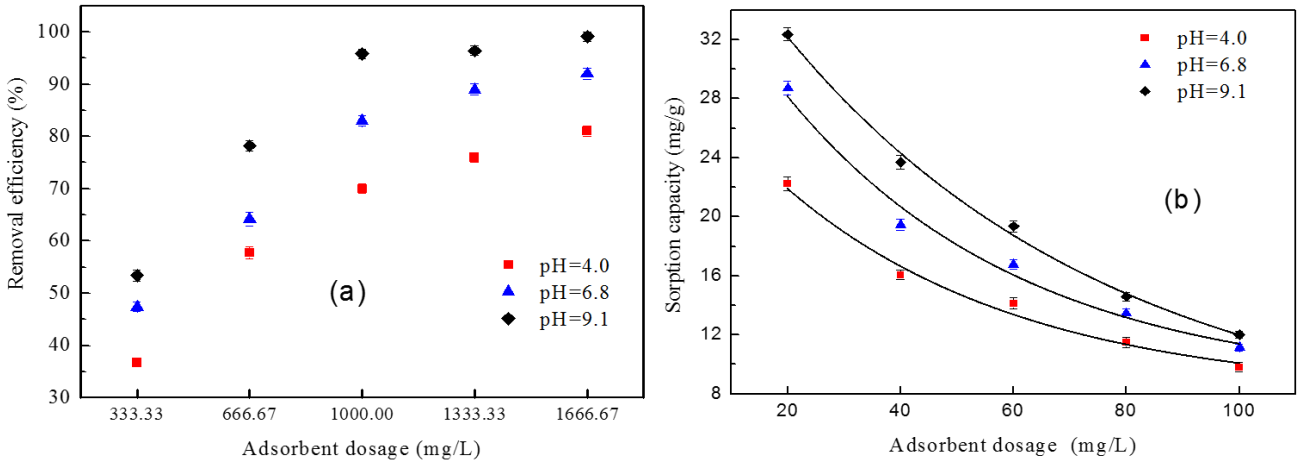

Fig. 5 Effect of the BSMU dosage and pH 4.0, 6.8, and 9.1 on (a) sorption removal efficiency and (b) sorption capacity. Solid line is fitting line of exponential decay model.

A comparison in sorption performance of antimony among biochar, MMOF and BSMU was made at pH 9.1, a BSMU dose of 1000 mg/L, stirring speed 150 rev/min, temperature 30 °C, sorption time 24 h and Sb (III) concentration 20 mg/L. The result is shown in supporting information (see Fig. S4). As illustrated in Fig. S4a, it showed that removal efficiency was 53% with biochar (sorption capacity=10.62 mg/g), 83% with MMOF (sorption capacity=16.63 mg/g), 92% with biochar supported MMOF (sorption capacity=18.43 mg/g). This demonstrated that the biochar supported MMOF increased the sorption performance of either MMOF or biochar alone. As previously indicated, the optimum proportion of components, the $R_{MMOF/Biochar}$ of the BSMU was 4:1, which reduces the amount of MMOF and optimizes both sorption and synthesis minimizing the MMOF needed with positive implications for reducing the costs of final application. The effect of sorption time in the range of 0.5 h to 24 h on sorption density was investigated, using pH 4.0, 6.8 and 9.1, a BSMU dose of 1000

mg/L and stirring speed 150 rev/min, temperature 303 K. The result is shown in Fig. S4b, where sorption equilibrium time was reached after only 4 h. After the sorption equilibrium, the sorption capacity did not change significantly, which indicated that antimony could not be released to the aqueous environment again, demonstrating the stability of bound antimony.

3.4 Effect of antimony concentration

The effect of three initial Sb (III) concentrations (10 mg/L, 30 mg/L and 50 mg/L) on sorption was investigated at pH 9.1, the BSMU dose of 1000 mg/L and stirring speed 150 rev/min, temperature 303 K. The result is shown in Fig. S5a-b. As expected, sorption increased with increasing antimony concentration and removal efficiency increased with sorption time. For example, at antimony 50 mg/L, the sorption capacity was up to 33.9 mg/g, and greater than that at 30 mg/L and 10 mg/L. With the increase of the concentration of antimony, the sorption tended to be saturated thus increasing sorption capacity. However, at higher concentrations the residual antimony was not removed and removal rate did not increase. At any concentration, the variation of adsorption capacity with adsorption time followed pseudo second order kinetic model. The details on the kinetics were discussed in the later section.

3.5 Influence of coexisting ions

The BSMU had a stronger resistance to the negative influence of co-existing anions. In general, the coexisting anions such as NO_3^-, Cl^-, SO_4^{2-}, F^-, and PO_4^{3-}, do not often inhibit Sb (III) sorption, seen for example with Sb (III) sorption onto bentonite (PO_4^{3-}, SO_4^{2-} and NO_3^-) (Xi et al., 2011), zirconium-based metal−organic frameworks (PO_4^{3-}, SO_4^{2-} F^-, and NO_3^-) (Li et al., 2017) and a tannin based adsorbent (Cl^-, PO_4^{3-}, SO_4^{2-} and NO_3^-) (Hugo et al., 2018). However, in the presence of iron-based materials, the influence of coexisting ions on Sb (III) sorption does occur. For example, the sorption

342 of Sb (III) by a Ce (III)-doped Fe_3O_4 magnetic particles, showed a minor influence from PO_4^{3-} while Cl^- and SO_4^{2-} enhanced
343 sorption effect (Qi et al., 2017). For an iron-based metal organic framework (Fe-MIL-88B), the PO_4^{3-} caused a 12 %
344 reduction in the removal of Sb (III)(Cheng et al., 2020). Furthermore, it was up to 30.43% for a chitosan supported Fe-MIL
345 metal organic frameworks (Xiong et al., 2020). In comparison, Sb(V) was affected significantly by competing anions,
346 especially PO_4^{3-}, reducing the efficiency of antimony removal (Xi et al., 2011; He et al., 2015). Although these iron-based
347 materials include both Fe (II) and Fe (III), it is difficult for the Sb (V) and Sb (III) to co-exist in the same system because
348 the presence of Fe (II) as a strong reducing agent preventing the oxidation of Sb (III) to Sb(V) and indirectly affecting
349 antimony sorption (Xiong et al., 2020). In this study, we examined the influence of coexisting anions on the sorption of Sb
350 (III) onto the BSMU. Our investigation was conducted at pH 9.1, a BSMU dose of 1000 mg/L and stirring speed 150
351 rev/min, temperature 303 K with coexisting ions including NO_3^-, Cl^-, SO_4^{2-}, and PO_4^{3-} . The ionic strength was in the range
352 0.01 M to 1.0 M. The result is shown in Fig. S6 which shows no significant ionic influence at all ionic strength. The PO_4^{3-}
353 had a relatively high negative influence compared to the other anions, followed by the SO_4^{2-}, but the degree of reduction
354 was not more than 5%. Therefore, the performance of BSMU was less influenced by coexisting ions, which has been
355 considered as an indicator of sorption influence by a specific binding or inner-sphere surface complex binding (Xi et al.,
356 2011).
357
358 **3.6 Sorption kinetics and isothermal analysis**
359 The sorption of antimony onto the BSMU followed the pseudo second-order kinetics rather than the pseudo first-order
360 kinetics as indicated by correlation coefficients (R^2). As illustrated in Fig. 6a-b and Table S2, good fit lines for pseudo
361 second-order kinetics at each antimony concentration yielded relatively high R^2 values up to over 0.98. Measured
362 equilibrium sorption capacity was in good agreement with calculated. On the contrary, poor fit to pseudo first-order kinetics

363 yielded R^2 values lower than 0.90 at each antimony concentration, which was significantly lower than the R^2 values derived
364 from the pseudo second-order kinetics model fit. This suggests that the sorption of antimony on the BSMU followed pseudo
365 second-order kinetics and antimony was absorbed onto the surface of the BSMU via chemical interaction.
366
367 The data for sorption of Sb (III) onto the BSMU was analysed using the Freundlich and Langmuir isotherm models at
368 temperatures from 297 K to 313 K, and degree of fit was assessed using the correlation coefficient. As shown in Fig. 6c-d
369 and Table S3, it showed that sorption data followed Freundlich isotherm model better as indicated by R^2 over 0.95 than
370 0.90 for Langmuir isotherm model, which suggested the sorption of antimony onto the BSMU was a multilayer sorption.
371 The Freundlich constant ($1/n$) is an indicator to determine whether it is favorable sorption (Zhao et al., 2010). The range
372 0.1 to 0.5 suggests a favorable sorption but a hard sorption when over 2.0 (Zhao et al., 2010). The $1/n$ constants for all
373 temperatures were all smaller than 0.5, indicating a favorable sorption and a high affinity between antimony and the BSMU.
374 The K_f was related to the sorption capacity (DuranoLu et al., 2012). With the increase of the temperature, the K_f increased,
375 showing the sorption was endothermic in nature. In comparison, the BSMU had the same sorption kinetics and isothermal
376 model as for the MMOF, which better followed pseudo second-order kinetics and the Freundlich sorption model (see Fig.
377 S7 and Table S4-5 in supporting information).

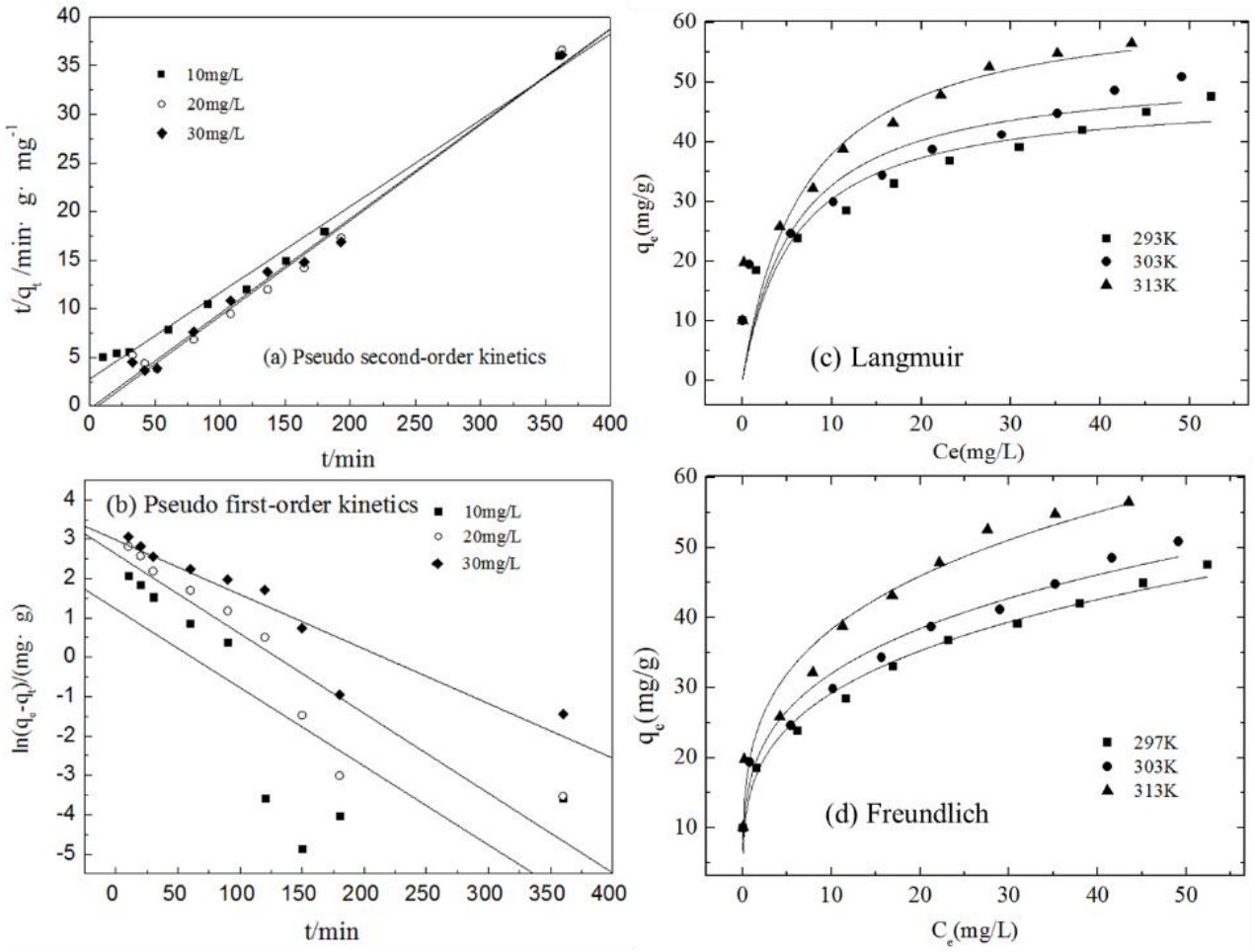

Fig. 6 Fit lines of sorption kinetics and isothermal models: (a) Pseudo second-order kinetics model, (b) Pseudo first-order kinetics model, (c) Langmuir isothermal model, and (d) Freundlich isothermal model

The sorption of antimony onto the BSMU was more sensitive to the temperature and consumed more energy than the adsorption with the MMOF. At temperatures 288 K to 313 K, sorption heat for antimony by the BSMU and the MMOF at Sb(III) concentration 20 mg/L, solution pH=9.1, sorption time 24 h, was investigated. As seen from ΔG^{θ} values shown in supporting information (see Table S6), the values are all negative, which suggested that the sorption with the BSMU and the MMOF were both thermodynamically spontaneous. It also showed that ΔG^{θ} of the sorption with the BSMU was more sensitive to the increase in temperature while for the MMOF it did not change significantly. The activation energy of sorption with the BSMU and the MMOF was 8.772 kJ/mol and 5.024 kJ/mol, respectively. Activation energy is usually

used as one of the criteria to distinguish physical sorption and chemical sorption, with physical sorption being easy to reverse and reaches equilibrium rapidly. Consequently the energy demand is very small, not more than 4.184 kJ/mol (Sag and Kutsal, 2000) because the forces involved are weak such as Weak van der Waals forces (Duranoğlu et al., 2012). Chemisorption has a non-activated and activated step for which the rate varies with temperature (Sag and Kutsal, 2000). From the results of our investigation, the activated chemisorption needs more activation energy and it can be seen that the energy required for the BSMU was higher than that needed for the MMOF, which was closer to the value for physical sorption. Therefore, antimony sorption by the BSMU would be driven by chemisorption. In detail, the ΔH^{θ} of chemical sorption is considered >29 kJ/mol and that of complexation is between 8 and 60 kJ/mol (Mungasavalli et al., 2007; Duranoğlu et al., 2012). A higher ΔH^{θ} =97.56 kJ/mol for the BSMU, suggested the sorption of Sb (III) onto the BSMU would be through a chemical sorption process. The ΔH^{θ} =21.44 kJ/mol for the MMOF indicated that the sorption would be driven by complexation. They are positive values showing their sorption was endothermic in nature. The positive value of the ΔS^{θ} =360 J/mol·K for the BSMU was three times larger than the ΔS^{θ} =113.72 J/mol·K for MMOF, implying the contact randomness between antimony and the BSMU increased. Overall, the sorption of Sb (III) onto BSMU is significantly different from onto the MMOF.

3.7 Analysis of Reaction Mechanism

Three steps could be identified from the overall sorption of antimony onto the BSMU, indicating that the sorption was controlled by either surface or intraparticle diffusion (Duranoğlu et al., 2012). If the q_t and $t^{0.5}$ is a linear relationship through zero, it suggests that the intraparticle diffusion is the sole rate-limiting step but the presence of changes in gradient suggests the sorption process also includes a complex chemical reaction (Russo et al., 2020). As seen from Fig. 7a, three stages are highlighted: a surface or film diffusion process (step 1), a gradual sorption (step 2) of intraparticle or pore

410 diffusion, and a final equilibrium (step 3) (Russo et al., 2020). Since it did not pass through the origin, the sorption of
411 antimony onto the BSMU was not only determined by a rate-limiting based intraparticle diffusion, but also by other
412 chemisorption processes. In comparison, the BSMU had the same sorption steps with the MMOF that the q_t and $t^{0.5}$ was a
413 linear relationship and fitted a three-stage process (see Fig. S8 in supporting information), showing the intraparticle
414 diffusion is not the only rate-limiting step to control the sorption of antimony onto MMOF.
415
416 The Sb(III) may exist in the form of uncharged and insoluble antimony hydroxide $Sb(OH)_3$ over a wide pH range (2-10.4)
417 in aqueous solutions (Ungureanu et al., 2015). Neutral charge $Sb(OH)_3$ inhibits electrostatic attraction, and new interaction
418 mechanisms are needed through a possible hydrogen bonding (Ungureanu et al., 2015; Xiong et al., 2020) or others such
419 as surface complexation (Vithanage et al., 2013). If the adsorbent was defined as $\equiv MeOH$ and the metal Sb was denoted
420 as M, the properties of the surface of the adsorbent change with pH because of reaction $\equiv MeOH + H^+ \leftrightarrow \equiv MeOH_2^+$ and
421 $\equiv MeOH \leftrightarrow \equiv MeO^- + H^+$. Variation of initial solution pH in the range of 3 to 11 during sorption without buffering
422 was tested in this study with the BSMU dose of 1200 mg/L, stirring speed 150 rev/min, temperature 303 K and sorption
423 time 24 h. The result is shown in supporting information (see Fig. S9). As illustrated in the figure, it showed that an initial
424 pH value increased after sorption at pH 6 or less and increased when at a pH equal or greater than 6.0. This shows that after
425 addition of the BSMU, H^+ was consumed by reaction with the sorbent so that the pH increased
426 ($\equiv MeOH + H^+ \leftrightarrow \equiv MeOH_2^+$ is the main reaction) but when the initial pH was lower than 6, further increasing the pH
427 value, the release of H^+ to solution decreased pH significantly ($\equiv MeOH \leftrightarrow \equiv MeO^- + H^+$ is the main reaction process).
428 Finally, allowing an effective interaction between $\equiv MeO^-$ and antimony thus enhancing the sorption efficiency.
429
430 The interaction occurring between oxygen and antimony in solution-surface interactions has been highlighted (Vithanage

et al., 2013; He et al., 2015; Li et al., 2017), and from analysis by FT-IR, X-ray photoelectron spectroscopy and Raman spectroscopy, the main sorption sites are attributed to hydroxyl and carboxyl functional groups. For example, through replacement of hydrogen, antimony could bound with oxygen of adsorbent (Vithanage et al., 2013). The FT-IR results of BSMU before and after sorption are shown in Fig. 7b. There were some significant peaks at 3423 cm^{-1}, 2930 cm^{-1}, 1617 cm^{-1}, 1577 cm^{-1},1494 cm^{-1}, 1384 cm^{-1}, 1043 cm^{-1}, 873 cm^{-1}, and 624 cm^{-1}. After sorption, these characteristic peaks showed significant changes: at 3423 cm^{-1} and 2930 cm^{-1}, corresponding to –NH and –OH (Zhang et al., 2011; Wang; et al., 2015), respectively, they moved towards low frequency and exhibited wider peak at all pH. This suggested the H of hydroxyl groups would be replaced by antimony species, –NH was protonated, $\equiv MeOH_2^+$ was formed, all of which would the reason for H^+ loss. The C-H and O-H at 1494 cm^{-1} and 1384 cm^{-1} (Sigma-Aldrich; Rodrigues et al., 2015), respectively, increased at pH 4.0 while decreased at pH 6.8 and pH 9.1. Under alkali condition, carboxyl ionization could enhance the link of negatively charged oxygen with antimony. It showed the peak at 599 cm^{-1} assigned to Fe–O vibration (Ting Wang, 2013; Wang; et al., 2015). After sorption, the peak moved toward low frequency to 593 cm^{-1} at pH 4.0, 595 cm^{-1} at pH 6.8, 595 cm^{-1} at pH 9.1. In addition, the Zr-O would also be a sorption sites as indicated by the XPS analysis (Li et al., 2017).

It was much effective for Sb (III) removal under an alkaline condition, which is inseparable from the binding of Sb and oxygen. The XPS results of a high-resolution scan of the O 1s of BSMU oxygen, and the Sb 3d of BSMU and Sb (III) reaction sample (denoted as BSMU-Sb) at pH 6.8 were used to provide insights to the adsorption mechanism. The results are shown in Fig. 7c-e. As illustrated in Fig. 7c the O 1s XPS spectra for BSMU, has two significant peaks appearing at around 531.7 and 530.3 electron volts (eV) which were fitted into three oxygen components including a lattice oxygen bond at 530.28 eV (O_{latt}), carbonyl (C = O) group oxygen or absorbed oxygen at 531.49 eV (O_{adc}), and a hydroxyl group oxygen at 531.84 eV (O_{OH}). As illustrated in Fig. 7d, the Sb 3d result of BSMU-Sb showed that the Sb 3d XPS peak was

split into Sb $3d_{3/2}$ and Sb $3d_{5/2}$ states corresponding to the Sb (III) oxide at around 540.1 eV and 530.6 eV, respectively, which showed that antimony can be adsorbed by the BSMU, which were divided into four Sb oxide compounds of which binding energy peak at 530.32 eV, 531.08 eV, 532.03 eV and 540.10 eV. The oxygen peaks position changed and new Sb $3d_{5/2}$ peaks generated, which showed that Sb and BSMU was successfully bonded. As illustrated in Fig. 7e, two significant Fe 2p peaks at 710.7 eV and 724.5 eV corresponded to the characteristic peaks of Fe_3O_4 (Im et al., 2015). While the Sb (III) can be oxidized to Sb (V) in the presence of some ambient oxygen, the binding energy signal peak of Sb (V) at a higher value (over 540.2 eV) did not occur in this study because the coexistence of Sb (V) and Fe (II) was not possible when $2Fe^{2+}+Sb^{5+}\rightarrow 2Fe^{3+}+Sb^{3+}$ where Fe (II) is strongly reductive and can react with Sb (V) thus preventing the oxidation of Sb (III) to Sb (V) (Huang et al., 2006). This results showed that the adsorption reaction existed in the absence of Sb (V).

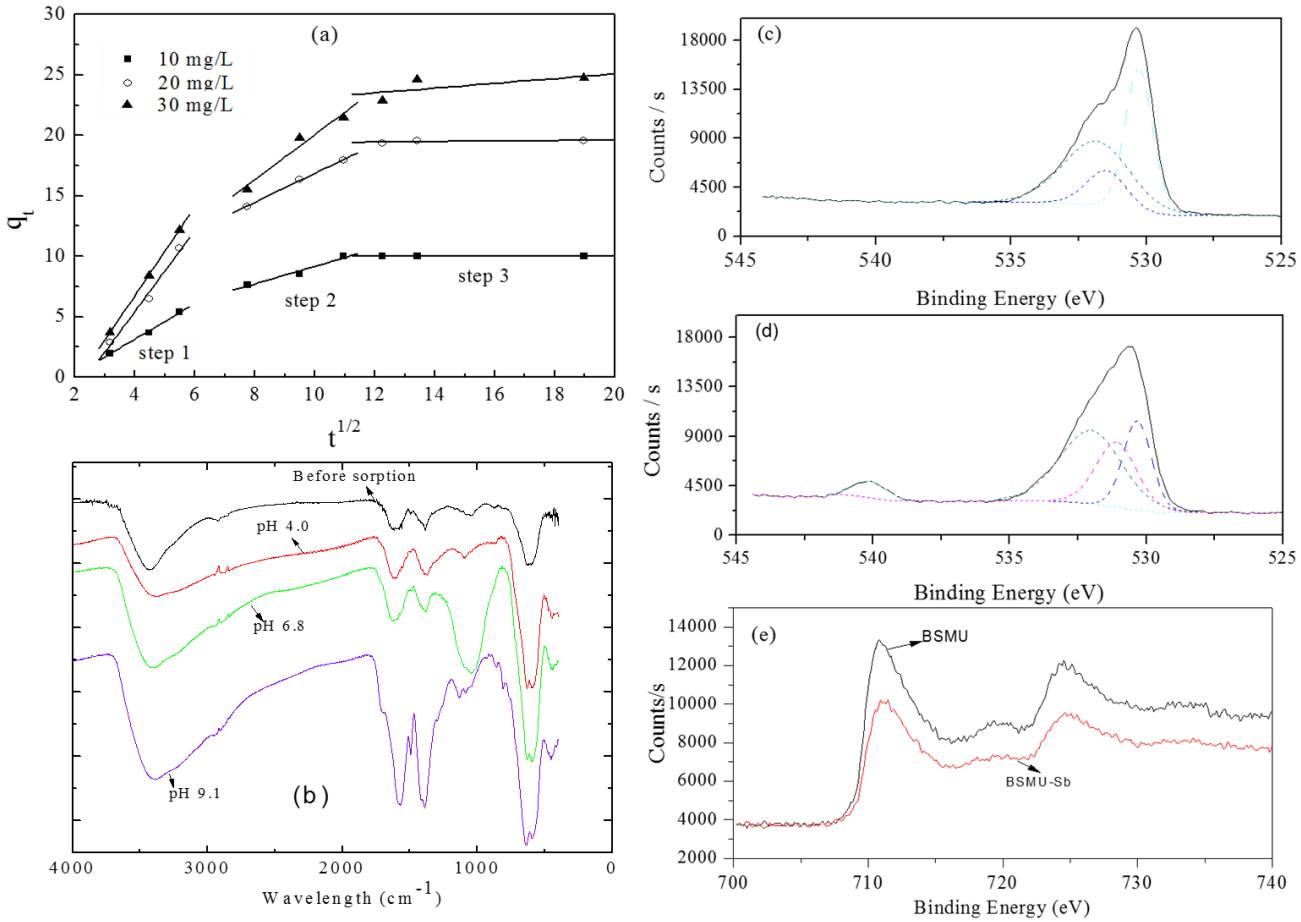

Fig. 7 Intraparticle diffusion plots for Sb (III) sorption on the BSMU at different adsorbent concentration

4 CONCLUSIONS

In this study, we evaluated the adsorption of mushroom biochar supported MMOF nanoparticles for removal Sb (III) from solution. It showed a great potential for enhancing the adsorption of Sb (III) with biochar or magnetic UIO-66-2COOH. The BSMU was demonstrated to be an effective composite adsorbent to remove Sb (III) and exhibited much higher removal capacity toward Sb (III) than biochar, MOF and MMOF. Through adsorption model and elemental analysis, it suggested that the chemical interaction between carboxyl (-COOH), hydroxyl (-OH), and amine (-NH) groups of absorbent and the Sb (III) species led the adsorption reaction. It has good application across different reaction conditions. Over a broad pH, it works well and is superior to the traditional adsorbent only in acidic conditions. The presence of coexisting ions has little effect on Sb (III) removal. Further studies of recycling and process scale up are needed to strengthen its practical application.

ACKNOWLEDGEMENTS

This work is financially supported by National Natural Science Foundation of China (No. 51408215 and No. 22002010) and Natural Science Foundation of Hunan Province of China (No. 2018JJ2128).

References

Afifi, E.E., Attallah, M.F., Borai, E.H., 2016. Utilization of natural hematite as reactive barrier for immobilization of radionuclides from radioactive liquid waste. J. Environ. Radioactiv 151, 156-165.

United States EPA, 2018, 2018 Edition of the Drinking Water Standards and Health Advisories, U.S. Environmental Protection Agency, Washington USA.

Alderton D., S.T., Bruns L., 2014. Distribution and mobility of arsenic and antimony at mine sites in fry Macedonia. Carpathian J. Earth Environ. Sci. 9, 43-56.

Asadabadi, S., Merati, Z. , 2021. A tailored magnetic composite synthesized by graphene oxide, chitosan and aminopolycarboxylic acid for diminishing dye contaminant. Cellulose 28, 2327–2351.

B. Gao, J. Lu, Zhou., H.D., 2012. The distribution, accumulation and potential source of seldom monitored trace elements

in sediments of Beijiang River, South China. Water Sci. Technol. 65, 2118-2124.

Bar, N., Retoux, R., Henry, J., ernay, B.B., Villemin], D., 2014. Partially phosphonated polyethylenimine-coated nanoparticles as convenient support for enzyme immobilization in bioprocessing. Sensor Actuat. B-Chem.192, 269-274.

Bo Wang, Y.Z., Xiao Feng, 2016. A method of preparing metal organic framework material film. Patent, Patent Number: 451 CN104710559B, China.

Cao, Y., 2019. Construction of Quality and Safety Management System of Edible Fungi Supply Chain in China. Edible Fungi of China 38, 27-29.

Chai, W.S., Cheun, J.Y., Kumar, P.S., Mubashir, M., Show, P.L., 2021. A review on conventional and novel materials towards heavy metal adsorption in wastewater treatment application. J. Clean Prod. 296, 126589.

Cheng, K., Wu, Y.-n., Zhang, B., Li, F., 2020. New insights into the removal of antimony from water using an iron-based metal-organic framework: adsorption behaviors and mechanisms. Colloids Surf. A Physicochem. Eng. Asp. 602, 125054.

Chew, K.W., Yap, J.Y., Show, P.L., Suan, N.H., Juan, J.C., Ling, T.C., Lee, D.J., Chang, J.S., 2017. Microalgae biorefinery: High value products perspectives. Bioresource. Technol. 229, 53-62.

Duranoğlu, D., Trochimczuk, A.W., Beker, U., 2012. Kinetics and thermodynamics of hexavalent chromium adsorption onto activated carbon derived from acrylonitrile-divinylbenzene copolymer. Chem. Eng. J. 187, 193-202.

A. Brenner, E.J. Hoekstra, 2012. Drinking Water Quality Standards and Regulations. IWA Publishing, London, 2012 .

WHO (World Health Organization), 2011. Guidelines for drinking-water quality ((Fourth Edition), WHO Press, Switzerland.

Fan, G., Zheng, X., Luo, J., Peng, H., Hui, L., Bao, M., Hong, L., Zhou, J., 2018. Rapid synthesis of Ag/AgCl@ZIF-8 as a highly efficient photocatalyst for degradation of acetaminophen under visible light. Chem. Eng. J. 351, 782-790.

Fan, Z., 2007. Determination of antimony(III) and total antimony by single-drop microextraction combined with electrothermal atomic absorption spectrometry. Anal. Chim. Acta 585, 300-304.

Fazal, T., Razzaq, A., Javed, F., Hafeez, A., Rehman, F., 2019. Integrating Adsorption and Photocatalysis: A cost effective Strategy for Textile Wastewater Treatment using Hybrid Biochar-TiO2 Composite. J. Hazard. Mater. 390, 121623.

Fu, Z., Wu, F., Amarasiriwardena, D., Mo, C., Liu, B., Jing, Z., Deng, Q., Liao, H., 2010. Antimony, arsenic and mercury in the aquatic environment and fish in a large antimony mining area in Hunan, China. Sci. Total Environ. 408, 3403-3410.

Guila-Almanza, E., Low, S.S., Hernández-Cocoletzi, H., Atonal-Sandoval, A., Show, P.L., 2021. Facile and green approach in managing sand crab carapace biowaste for obtention of high deacetylation percentage chitosan. J Environ. Chem. Eng. 9, 105229.

Hao, N., Cao, J., Ye, J., Zhang, C., Li, C., Bate, B., 2021. Content and morphology of lead remediated by activated carbon and biochar: A spectral induced polarization study. J. Hazard. Mater. 411, 124605.

Hatefi R., K.K., Shahsavari A. A., Asadian F., 2013. Investigation of Antimony contamination in groudwater resources : a case study. Esaim Proceedings 4, 181-198.

He, Z., Liu, R., Liu, H., Qu, J., 2015. Adsorption of Sb(III) and Sb(V) on Freshly Prepared Ferric Hydroxide (FeOxHy). Environ. Eng. Sci. 32, 95-102.

Hernández-Cocoletzi, H., Salinas, R.A., Guila-Almanza, E., Rubio-Rosas, E., Show, P.L., 2020. Natural hydroxyapatite from fishbone waste for the rapid adsorption of heavy metals of aqueous effluent. Environ. Technol. Inno. 20, 101109.

Hiller E., Lalinská B., Chovan M., Jurkovič Ľ., Klimko T., Jankulár M., Hovorič R., Šottník P., Fľaková R. and Ženišová Z.,2012. Arsenic and antimony contamination of waters, stream sediments and soils in the vicinity of abandoned antimony mines in the Western Carpathians, Slovakia. Appl. Geochemistry. 27, 598-614.

Huang, Y., RUIZ, Patricio, 2006. The nature of antimony-enriched surface layer of Fe-Sb mixed oxides. Appl. Surf. Sci. 252, 7849-7855.

Hugo, B., R.C, V.B., C.R, S.S., A.R, B.R., M.S., B.C., 2018. Recovery and valorization of tannins from a forest waste as an adsorbent for antimony uptake. J. Clean. Prod. 198, 1324-1335.

Huong, D., Chai, W.S., Show, P.L., Lin, Y.L., Chang, Y.K., 2020. Removal of cationic dye waste by nanofiber membrane immobilized with waste proteins. Int. J. Biol. Macromol 164, 3873-3884.

Im, M.E., Pham-Cong, D., Kim, J.Y., Choi, H.S., Kim, J.H., Kim, J.P., Kim, J., Jeong, S.Y., Cho, C.R., 2015. Enhanced electrochemical performance of template-free carbon-coated iron(II, III) oxide hollow nanofibers as anode material for lithium-ion batteries. J. Power Sources 284, 392-399.

Leong, Y.K., Show, P.L., Ooi, C.W., Ling, T.C., Lan, C.W., 2014. Current trends in polyhydroxyalkanoates (PHAs) biosynthesis: Insights from the recombinant Escherichia coli. J. Biotechnol. 180, 52-65.

Li, J., Li, Q., Qian, C., Wang, X., Lan, Y., Wang, B., Yin, W., 2019. Volatile organic compounds analysis and characterization on activated biochar prepared from rice husk. Int. J. Environ. Sci. Technol. (Tehran) 16, 7653-7662.

Li, J., Li, X., Hayat, T., Alsaedi, A., Chen, C., 2017. Screening of Zirconium-Based Metal-Organic Frameworks for Efficient Simultaneous Removal of Antimonite (Sb(III)) and Antimonate (Sb(V)) from Aqueous Solution. ACS Sustain. Chem. Eng. 5, 11496-11503.

Lin, T.Y., Chai, W.S., Chen, S.J., Shih, J.Y., Chang, Y.K., 2020. Removal of soluble microbial products and dyes using heavy metal wastes decorated on eggshell. Chemosphere, 128615.

Linbing Sun, Y.L., Xiaoqin Liu, 2019. Preparation and application of high stability monovalent copper modified metal 500 organic framework material. Patent, Patent Number: CN110314653A, China.

Luo, J., Luo, X., Crittenden, J., Qu, J., Bai, Y., Peng, Y., Li, J., 2015. Removal of Antimonite (Sb(III)) and Antimonate (Sb(V)) from Aqueous Solution Using Carbon Nanofibers That Are Decorated with Zirconium Oxide (ZrO_2). Environ. Sci. Technol. 49, 11115-11124.

553 Mubashir, M., Dumée, L., Fong, Y.Y., Jusoh, N., Show, P.L., 2021. Cellulose acetate-based membranes by interfacial
554 engineering and integration of ZIF-62 glass nanoparticles for CO_2 separation. J. Hazard. Mater., 125639.
555 Mungasavalli, D.P., Viraraghavan, T., Jin, Y.C., 2007. Biosorption of chromium from aqueous solutions by pretreated
556 Aspergillus niger: Batch and column studies. Colloids Surf. A Physicochem. Eng. Asp. 301, 214-223.
557 Nagarajan, D., Lee, D.J., Chen, C.Y., Chang, J.S., 2020. Resource recovery from wastewaters using microalgae-based
558 approaches: A circular bioeconomy perspective. Bioresource Technol. 302, 122817.
559 O"Neill, D., L., H. Zhang , Bradshaw, D., 2010. Macro-microporous MOF composite beads. J. Mater. Chem. 20, 5720-
560 5726.
561 Pehlivan, E., Cetin, S., 2009. Sorption of Cr(VI) ions on two Lewatit-anion exchange resins and their quantitative
562 determination using UV–visible spectrophotometer. J. Hazard. Mater. 163, 448-453.
563 Perez, G.P., Dumont, M. J., 2020. Production of HMF in high yield using a low cost and recyclable carbonaceous catalyst.
564 Chem. Eng. J. 382, 122766.
565 Qi, Z., Joshi, T.P., Liu, R., Liu, H., Qu, J., 2017. Synthesis of Ce(III)-doped Fe_3O_4 magnetic particles for efficient removal
566 of antimony from aqueous solution. J. Hazard. Mater. 329, 193-204.
567 Ritchie, V.J., Ilgen, A.G., Mueller, S.H., Trainor, T.P., Goldfarb, R.J., 2013. Mobility and chemical fate of antimony and
568 arsenic in historic mining environments of the Kantishna Hills district, Denali National Park and Preserve, Alaska. Chem.
569 Geol. 335, 172-188.
570 Rodrigues, C.V., Correa, J.R., Aiube, C.M., Andrade, L.P., Galv?O, P.M., Costa, P.A., Campos, A.L., Pereira, A.J., Ghesti,
571 G.F., Felix, J.F., 2015. Down- and Up-Conversion Photoluminescence of Carbon-Dots from Brewing Industry Waste:
572 Application in Live Cell-Imaging Experiments. J. Braz. Chem. Soc. 26, 2623-2628.
573 Russo, V., Rossano, C., Salucci, E., Tesser, R., Serio, M., 2020. Intraparticle diffusion model to determine the intrinsic
574 kinetics of ethyl levulinate synthesis promoted by Amberlyst-15. Chem. Eng. Sci., 115974.
575 S.S. Cameotra, Dhanjal, S., 2010. Environmental Nanotechnology: Nanoparticles for Bioremediation of Toxic Pollutants.
576 Bioremediat. J., 348-374.
577 Sag, Y., Kutsal, T., 2000. Determination of the biosorption activation energies of heavy metal ions on Zoogloea ramigera
578 and Rhizopus arrhizus. Process Biochem. 35, 801-807.
579 Seoane, B., Castellanos, S., Dikhtiarenko, A., Kapteijn, F., Gascon, J., 2016. Multi-Scale Crystal Engineering of Metal
580 Organic Frameworks. Coord. Chem. Rev. 307, 147-187.
581 Aldrich, Infrared spectrum Chart. htt ps://www.sigmaaldrich.com/china mainland/technical 531
582 documents/articles/biology/ir-spectrum-table.html.
583 Sohi, S.P., Krull, E., Lopez-Capel, E., Bol, R., 2010. A Review of Biochar and Its Use and Function in Soil. Adv. Agron.
584 105, 47-82.

585 Ssrab, D., D, C., Nmy, A., Man, K., Pls, E., Ckc, F., Dkw, G., Wen, D., D , J., 2020. Optimum interaction of light intensity
586 and CO_2 concentration in bioremediating N-rich real wastewater via assimilation into attached microalgal biomass as
587 the feedstock for biodiesel production - ScienceDirect. Process Saf. Environ. 141, 355-365.
588 Tan, Y., Chen, M., Hao, Y., 2012. High efficient removal of Pb(II) by amino-functionalized Fe_3O_4 magnetic nano-particles.
589 Chem. Eng. J. 191, 104-111.
590 Ting Wang, L.Z., Haiying Wang, Weichun Yang, Yingchun Fu, Wenli Zhou, Wanting Yu, Kaisong Xiang, Zhen Su, Shuo
591 Dai, and Liyuan Chai, 2013. Controllable synthesis of hierarchical porous Fe_3O_4 particles mediated by poly-
592 (diallyldimethylammonium chloride) and their application in arsenic removal. ACS Appl. Mater. Interfaces. 5,
593 12449−12459.
594 Ungureanu, G., Santos, S., Rui, B., Botelho, C., 2015. Arsenic and antimony in water and wastewater: Overview of removal
595 techniques with special reference to latest advances in adsorption. J. Environ. Manage. 151, 326-342.
596 Vieth, J.K., Janiak, C., 2010. MOFs, MILs and more: concepts, properties and applications for porous coordination
597 networks (PCNs). New J. Chem. 34, 2366-2388.
598 Vithanage, M., Rajapaksha, A.U., Dou, X., Bolan, N.S., Yang, J.E., Ok, Y.S., 2013. Surface complexation modeling and
599 spectroscopic evidence of antimony adsorption on iron-oxide-rich red earth soils. J. Colloid Interface Sci. 406, 217-224.
600 Wang, X., He, M., Xi, J., Lu, X., 2011. Antimony distribution and mobility in rivers around the world's largest antimony
601 mine of Xikuangshan, Hunan Province, China. Microchem. J. 97, 4-11.
602 Wang, Y., Ho, S.H., Cheng, C.L., Guo, W.Q., Chang, J.S., 2016. Perspectives on the feasibility of using microalgae for
603 industrial wastewater treatment. Bioresource Technol. 222, 485-497.
604 Wang;, T., Zhang;, L., Li;, C., Yang;, W., Song;, T., Tang;, C., Meng;, Y., Dai;, S., Wang;, H., Chai;, L., Luo, J., 2015.
605 Synthesis of Core-Shell Magnetic Fe_3O_4@poly(m-Phenylenediamine) Particles for Chromium Reduction and
606 Adsorption. Environ. Sci. Technol. 49, 5654-5662.
607 Wen, Y., Hai-cheng, L., Jia-wei, C., Yao-liang, S., Wei, C., 2018. Removal of Humic Acid from Water by Magnetic
608 Chitosan-Grafted Polyacrylamide. Environ. Sci. (Chinese) 39, 5532-5540.
609 Xi, J., He, M., Lin, C., 2011. Adsorption of antimony(III) and antimony(V) on bentonite: Kinetics, thermodynamics and
610 anion competition. Microchem. J. 97, 85-91.
611 Xie, W., Wan, F., 2019. Immobilization of polyoxometalate-based sulfonated ionic liquids on UiO-66-2COOH metal-
612 organic frameworks for biodiesel production via one-pot transesterification-esterification of acidic vegetable oils. Chem.
613 Eng. J. 365: 40-50.
614 Xiong, N., Wan, P., Zhu, G., Xie, F., Xu, S., Zhu, C., Hursthouse, A.S., 2020. Sb (III) removal from aqueous solution by a
615 novel nano-modified chitosan (NMCS). Sep. Purif. Technol. 236, 116266.
616 Xu, W., Wang, H., Liu, R., Zhao, X., Qu, J., 2011. The mechanism of antimony(III) removal and its reactions on the surfaces

of Fe-Mn binary oxide. J. Colloid Interface Sci. 363, 320-326.

Yang, H., Wang, B., Cheng, J., Wang, R., Zhang, S., Dong, S., Wei, S., Wang, P., Li, J.-R., 2019. Determination and removal of clenbuterol with a stable fluorescent zirconium (IV)-based metal organic framework. Microchim. Acta 186, 1-8.

Yao, S., Zhu, X., Wang, Y., Zhang, D., Wang, S., Jia, Y., 2020. Simultaneous oxidation and removal of Sb(Ⅲ) from water by using synthesized CTAB/$MnFe_2O_4$/MnO_2 composite. Chemosphere 245, 125601.125601-125601.125609.

Yunchun Liu, Q.W., 2018. Preparation and application of metal organic framework complex chromatographic materials. 569 Patent, Patent Number: CN201810435494.4, China.

Zhang, L.Y., Chai, L.Y., Liu, J., Wang, H.Y., Yu, W.T., Sang, P.L., 2011. pH manipulation: A facile method for lowering oxidation state and keeping good yield of poly (m-phenylenediamine) and its powerful Ag^+ adsorption ability. Langmuir 27, 13729-13738.

Zhao, Xudong, Liu, Dahuan, Huang, Hongliang, Zhong, Chongli, 2016. Highly selective and sensitive metal-organic framework fluorescent probe for Cu^{2+} through rational design of binding sites. Micropor. Mesopor. Mat. 224, 149-154.

Zhao, Z., Wang, X., Zhao, C., Zhu, X., Du, S., 2010. Adsorption and desorption of antimony acetate on sodium montmorillonite. J. Colloid Interface Sci. 345, 154-159.

Zhenyu Lou, X.X., Mengnan Huang, Weijun Shan, Ying Xiong, 2021. Preparation and application of a metal organic framework material modified by polyunsaturated carboxylic acid. Patent, Patent Number: CN201810860476.0, China.

Zhu, G., Bian, Y., Hursthouse, A.S., Xu, S., Xiong, N., Wan, P., 2020. The role of magnetic MOFs nanoparticles in enhanced iron coagulation of aquatic dissolved organic matter. Chemosphere 247, 125921.

Zhu, H.Y., Jiang, R., Xiao, L., Zeng, G.M., 2010. Preparation, characterization, adsorption kinetics and thermodynamics of novel magnetic chitosan enwrapping nanosized γ-Fe_2O_3 and multi-walled carbon nanotubes with enhanced adsorption properties for methyl orange. Bioresour. Technol. 101, 5063-5069.

Supporting information

Text S1

The used chemicals, mainly included ascorbic acid and potassium bromide, were purchased from Kemiou Chemical Reagent Co. (Tianjin, China). Hydrochloric acid (HCl) and concentrated sulfuric acid (H_2SO_4) were purchased from Zhuzhou Xingkong Chemical Co. (Zhuzhou, China). Ferrous sulfate, sodium salt trihydrate, 1, 10-Phenanthroline monohydrate, acetic acid, ammonium hydroxide, and sodium acetate anhydrous came from Sinopharm Chemical Reagent Co. (Shanghai, China). Anhydrous ethanol came from Hunan Huihong Reagent Co., Ltd (Hunan, China).

Text S2

Fe_3O_4 nanoparticles (nano-Fe_3O_4) were prepared using a solvothermal reduction by the following procedure: 1.62 g of $FeCl_3.6H_2O$ and 4.32 g of $C_2H_3NaO_2$ were dissolved in 60 mL of ethylene glycol, which was stirred at room temperature for 30 mins until a homogeneous solution was achieved. The solution was subsequently transferred to a polytetrafluoroethylene (PTFE)-lined autoclave to maintain reaction at 200 ºC for 8 hours. The solid products were separated under an external magnetic field at room temperature and then washed three times with ultra-pure water and ethanol. After vacuum drying for 24 hours at 60 ºC, the nano-Fe_3O_4 was produced.

Text S3

MOF (UiO-66-2COOH) was prepared by using the hydrothermal method following the process developed by our publish[25]: the materials with the molar ratio of $ZrCl_4$, BTEC and ultra-pure water (50.4 g) at 1:1.7:280 were mixed and was treated by a reflux heating for 24 hours at 100 ºC. When it was cooled to room temperature, white gel was washed repeatedly with ultra-pure water for removal of the excess acids and then re-dispersed in ultra-pure water for 16 hours to

undergo reflux heating at 100 ºC. Then, the product was centrifuged and washed three times with ethanol and water. After vacuum drying for 24 hours at 60 ºC, the MOF was obtained. The nano-Fe_3O_4 was further modified by a silica core shell through the Stober method using the following procedure: 1.0 g of Nano-Fe_3O_4 and 320 mL of ethanol were dispersed in 80 mL of water. The solution then underwent ultrasonic dispersion for 30 min, prior to the addition of ammonia hydroxide solution (5 mL). After mechanical stirring for 15 minutes, 20 ml of TEOS was slowly added 5 ml at a time every three hours, which maintained a reaction while being stirred under nitrogen for 18 hours at 50ºC. Then, the MOF was mixed with nano-Fe_3O_4 at their mass ratio 1:2 and stirred in water bath at 50 ºC for 6 hours. Finally, the product was collected with an external magnetic field and washed three times with ethanol and water. After vacuum drying for 24 hours at 60ºC, the magnetic MOF (MMOF) was obtained.

Table

Table S**1** Fitting parameters of Sb (III) sorption capacity vs. adsorbent coagulant dosage by exponential decay model

pH value	Exponential Decay Model Parameters			
	Amplitude constant (a)	Decay constant (k)	Offset value (b)	R^2
4.0	38.162	57.984	5.189	0.998
6.8	31.786	41.974	8.447	0.986
9.1	22.416	42.156	7.975	0.986

Table S**2** Fitting results of Sb (III) sorption onto the BSMU at various antimony concentration by kinetics models

Adsorbent C_0 (mg/L)	**Measured**	**Pseudo first-order kinetics**			**Pseudo second-order kinetics**		
	q_e (mg/g)	**Calculated q_e**	**k_1**	**R^2**	**Calculated q_e**	**k_2**	**R^2**

10	9.99	7.17	-0.02	0.58	8.94	0.09	0.99
20	19.50	16.90	-0.02	0.85	18.51	0.04	0.98
30	24.52	23.65	-0.01	0.87	23.70	0.03	0.99

Table S3 Fitting results of Sb (III) sorption onto the BSMU at various temperature by isothermal model

Adsorbent	**Isothermal model**	**Temperature (K)**	**Calculated q_{max}**	**b**	**R^2**
		297	48.26	0.17	0.67
	Langmuir	303	52.24	0.17	0.76
		313	64.05	0.15	0.78
Adsorbent		**Temperature (K)**	**K_F**	**1/*n***	**R^2**
		297	15.62	0.27	0.96
	Freundlich	303	17.49	0.26	0.97
		313	21.02	0.26	0.96

Table S4 Fitting results of Sb (III) sorption onto the MMOF at various antimony concentration by kinetics models

Adsorbent	C_0 (mg/L)	Measured q_e (mg/g)	Pseudo-first-order kinetics			Pseudo-second-order kinetics		
			Calculated q_e	k_1	R^2	Calculated q_e	k_2	R^2
MMOF	10	9.6604	8.7178	-0.0222	0.7749	10.4283	0.0813	0.9060
	20	18.9283	17.3666	-0.0176	0.8016	19.9683	0.0422	0.8926
	30	22.7489	21.1509	-0.0217	0.9404	23.7320	0.0370	0.9724

Table S5 Fitting results of Sb (III) sorption onto the MMOF at various temperature by isothermal model

Adsorbent	Isothermal model	Temperature (K)	Calculated q_{max}	b	R^2
MMOF	Langmuir	293	45.4838	0.17117	0.8476
		303	54.2024	0.11028	0.8061
		313	62.7790	0.13042	0.8925
		Temperature (K)	K_F	1/*n*	R^2
	Freundlich	293	12.8158	0.3113	0.9776
		303	12.9808	0.3356	0.9568
		313	15.4228	0.3428	0.9728

Table S6 Thermodynamic parameters for sorption of Sb (III) onto adsorbents

Adsorbents	C_0 /mg·L^{-1}	E_a kJ/mol	$\triangle S^{\theta}$ J/mol·K	$\triangle H^{\theta}$ kJ/mol	$\triangle G^{\theta}$/kJ·mol-1 288K	293K	303K	313K
BSMU	20	8.77	360	97.56	-12.28	-13.71	-20.81	-21.57
MMOF	20	5.02	113.71	21.44	-	-11.54	-13.749	-13.76

Figure

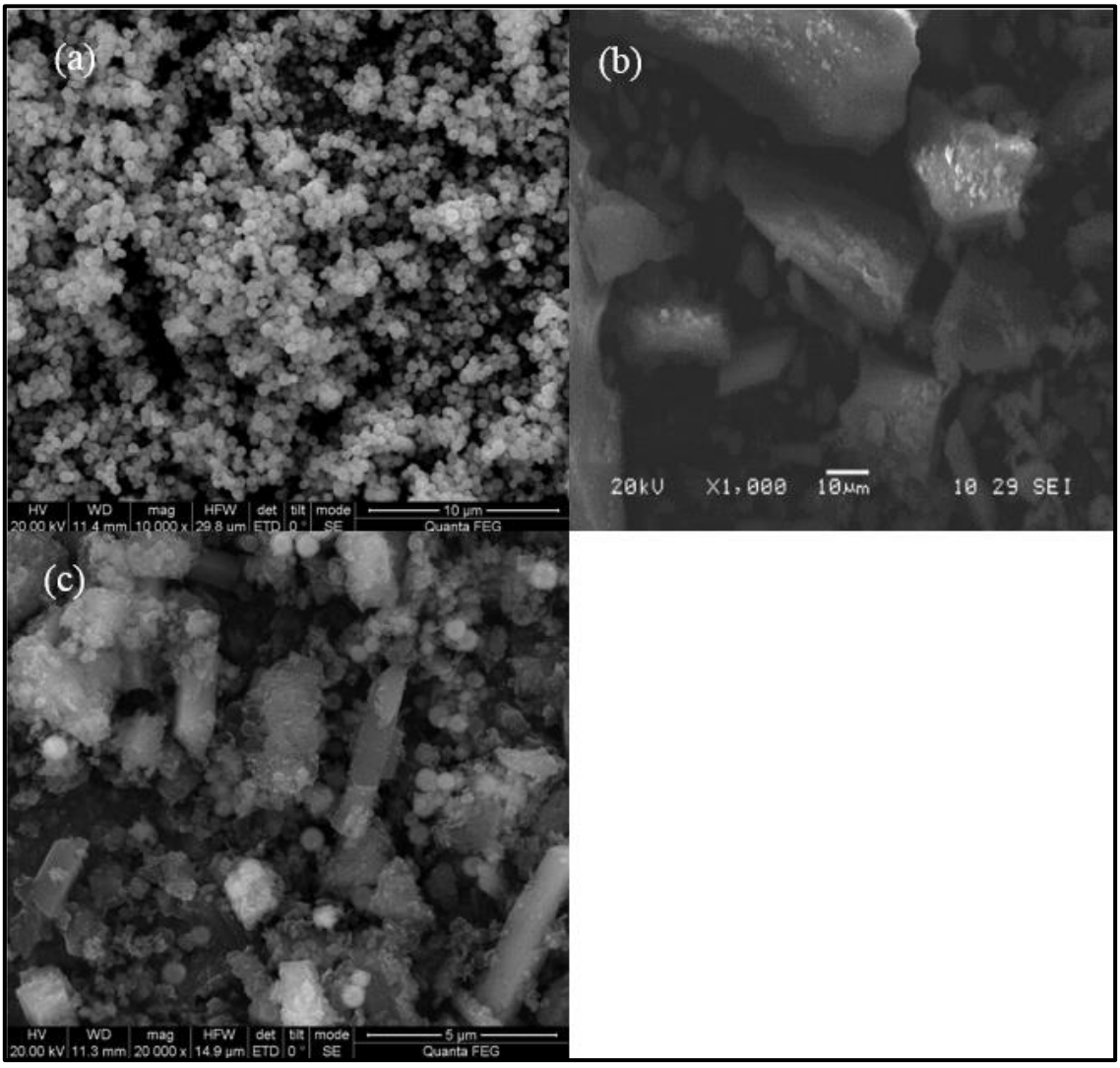

Fig. S1 SEM photographs for (a) nano-Fe_3O_4, (b) MOFs, (c) MMOF

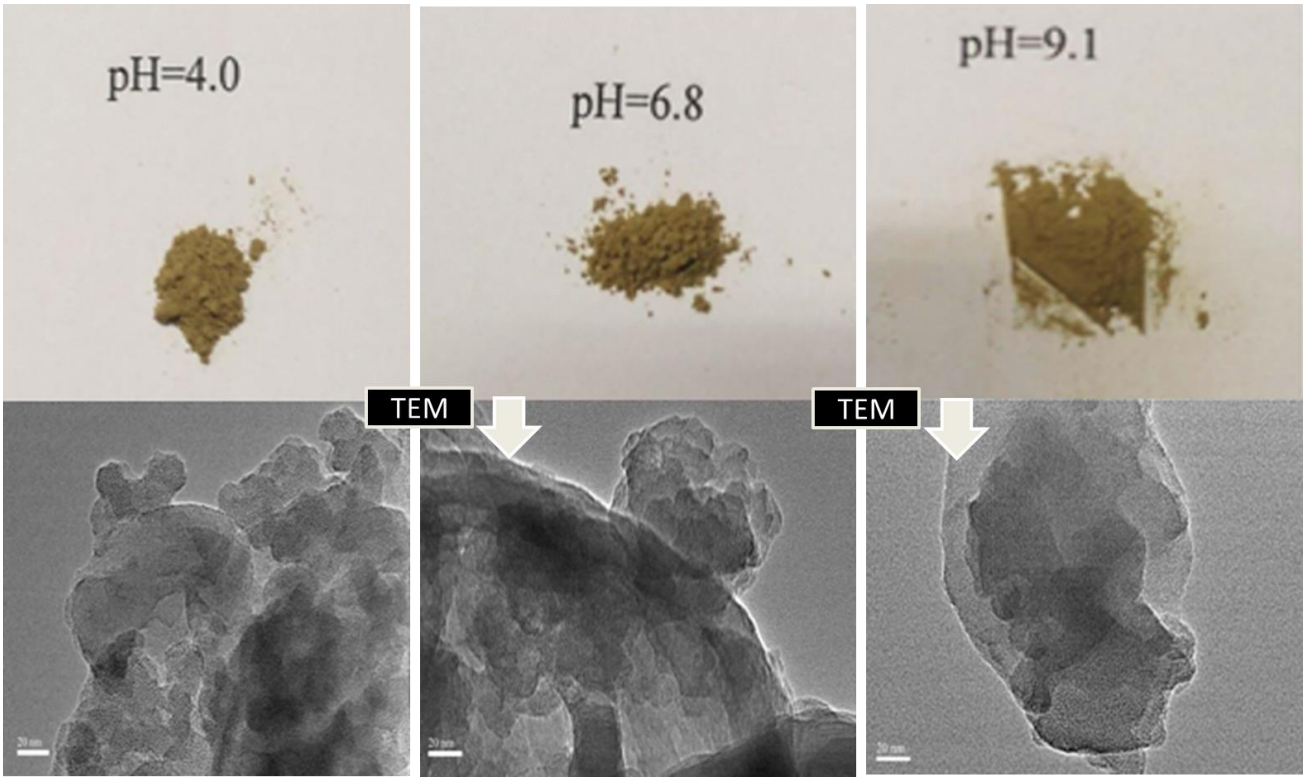

Fig. S2 TEM results of MOF in different pH conditions

Fig. S3 Photographs for BSMU prepared in the absence/presence of initiator. The results showed that without the initiator the dispersion and stability of the BSMU was not good. The enhanced initiator concentrations enhanced the quality

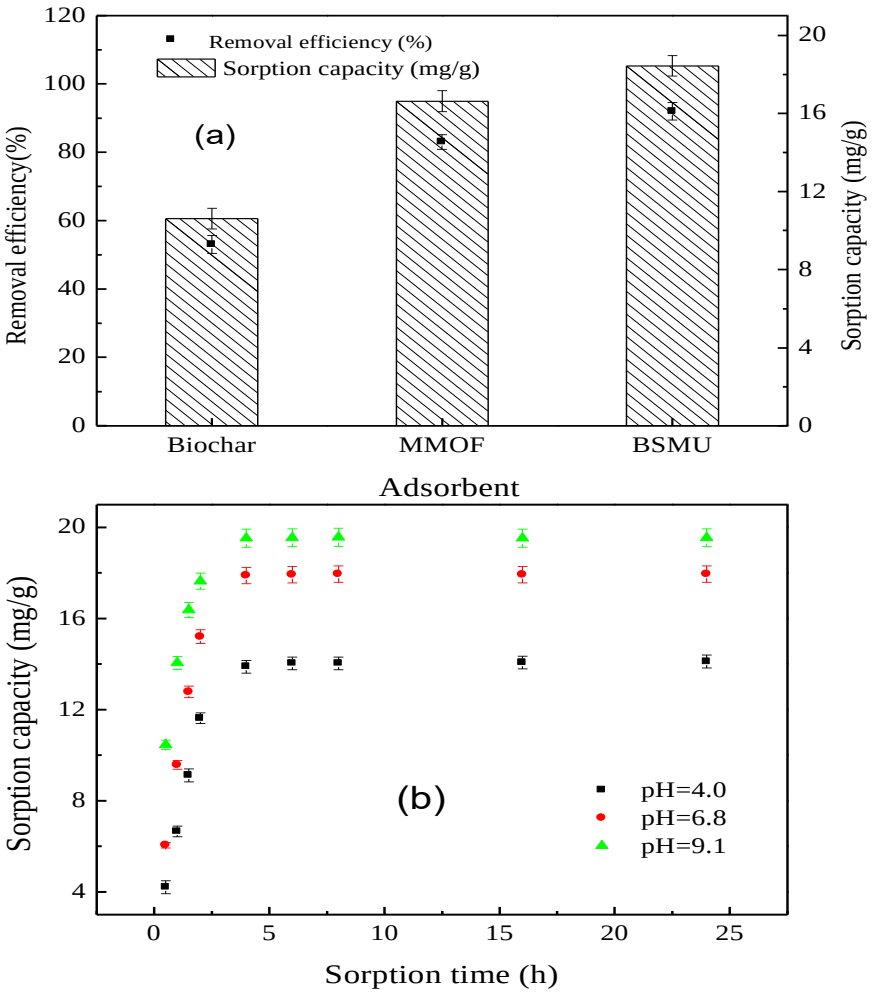

Fig. S4 (a) Comparison of adsorbents in sorption performance of Sb (III) and (b) effect of sorption time on sorption performance

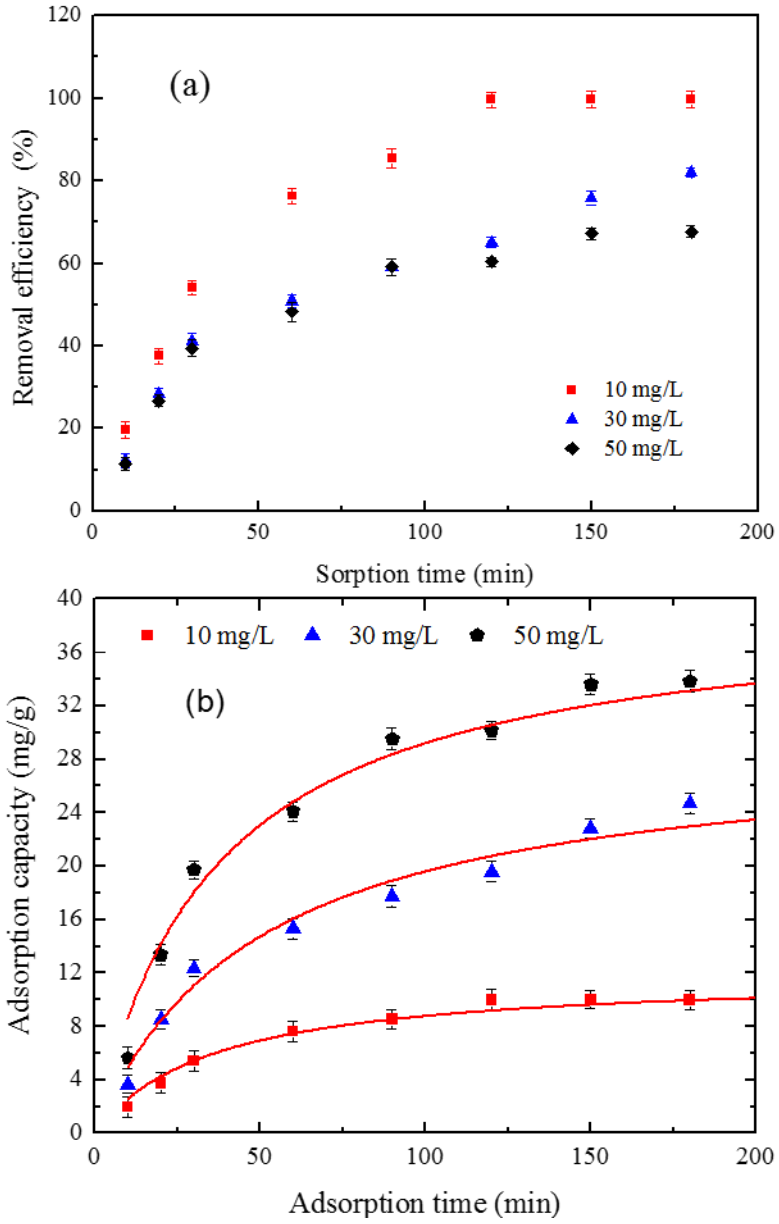

Fig. S5 Effect of antimony concentration on (a) sorption removal efficiency and (b) sorption capacity. Solid line is fitting line of pseudo second-order kinetics model.

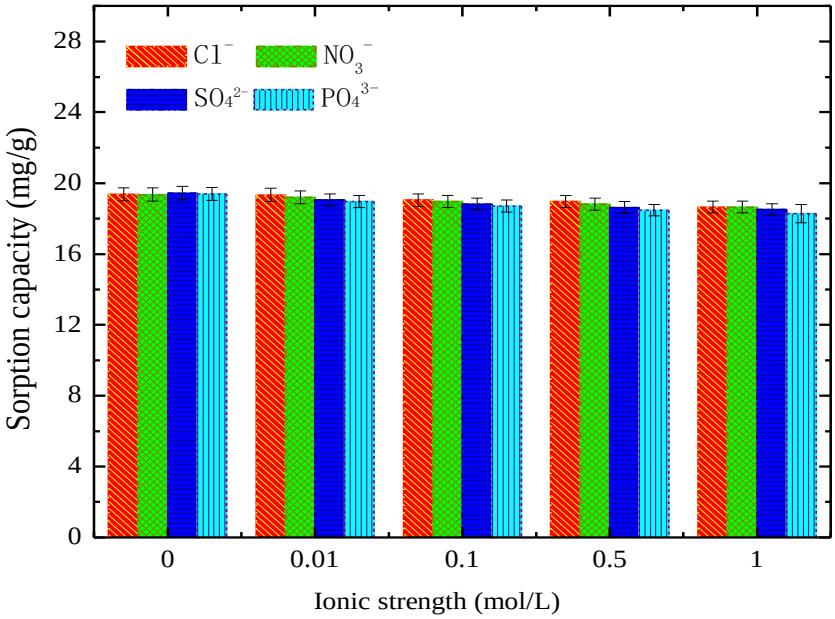

Fig. S6 Effect of coexisting ions on sorption capacity of Sb (III)

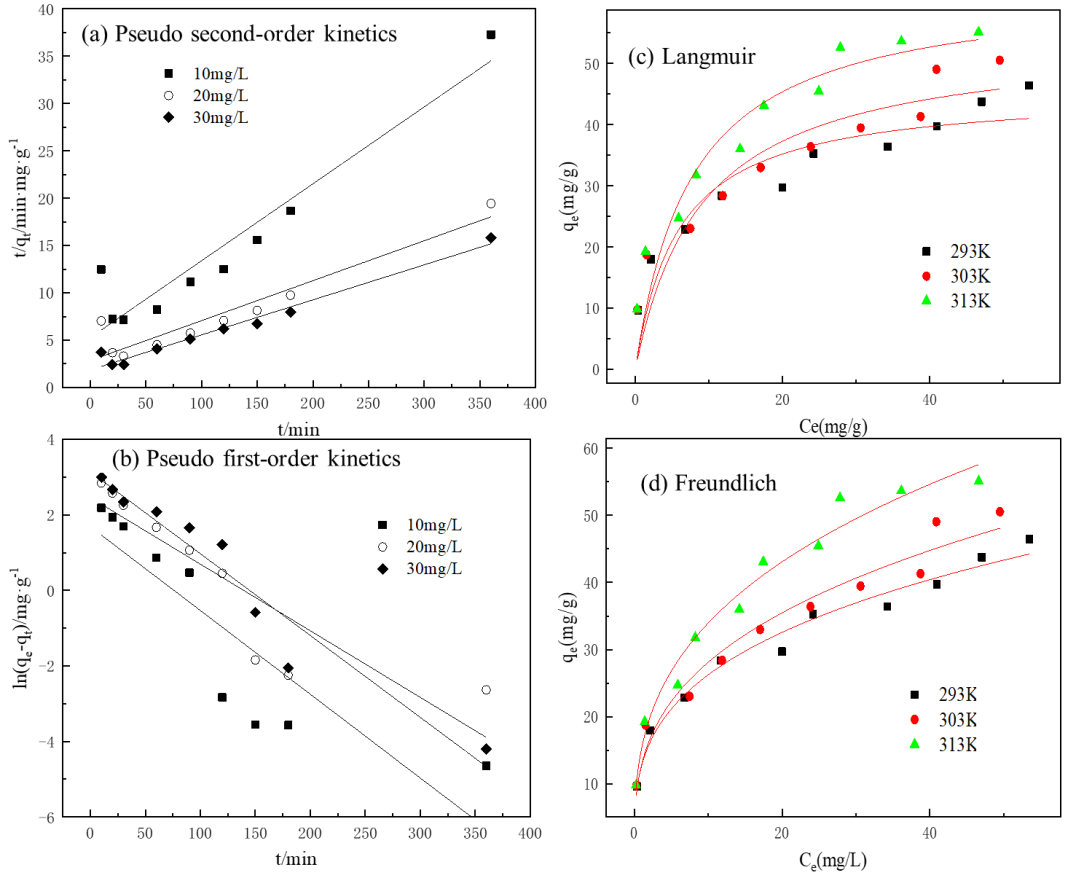

Fig. S7 The fitting results of Sb (III) sorption onto the MMOF at various antimony concentration by the models: (a) Pseudo second-order kinetics and (b) Pseudo first-order kinetics. The fitting results of Sb (III) sorption onto the BSMU at various

antimony concentration by the models: (c) Langmuir isothermal model, and (d) Freundlich isothermal model

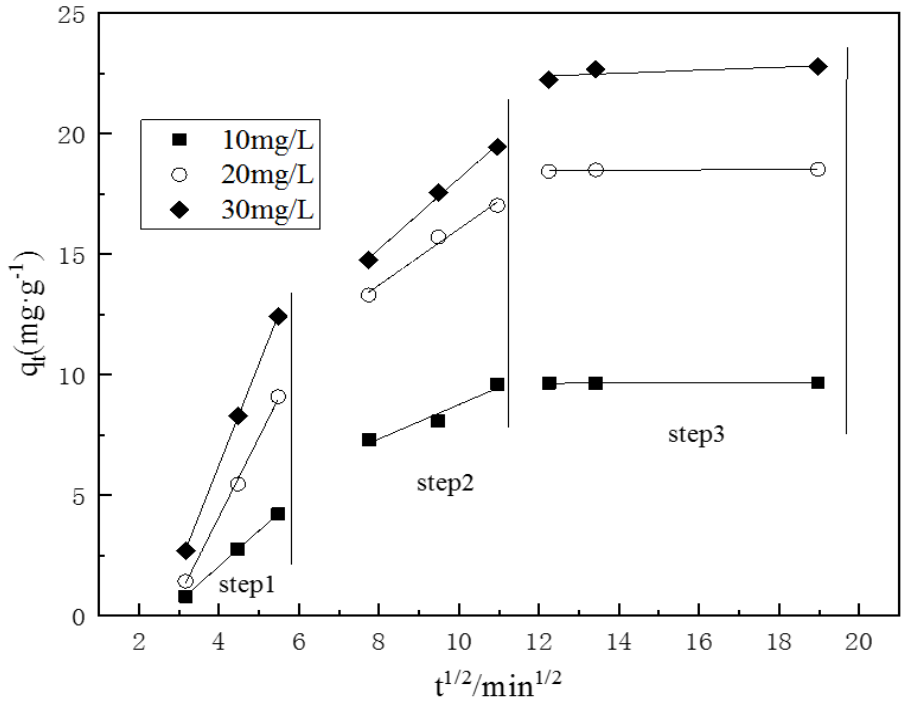

Fig. S8 Intraparticle diffusion plots for Sb (III) adsorption on the MMOF at different antimony concentration

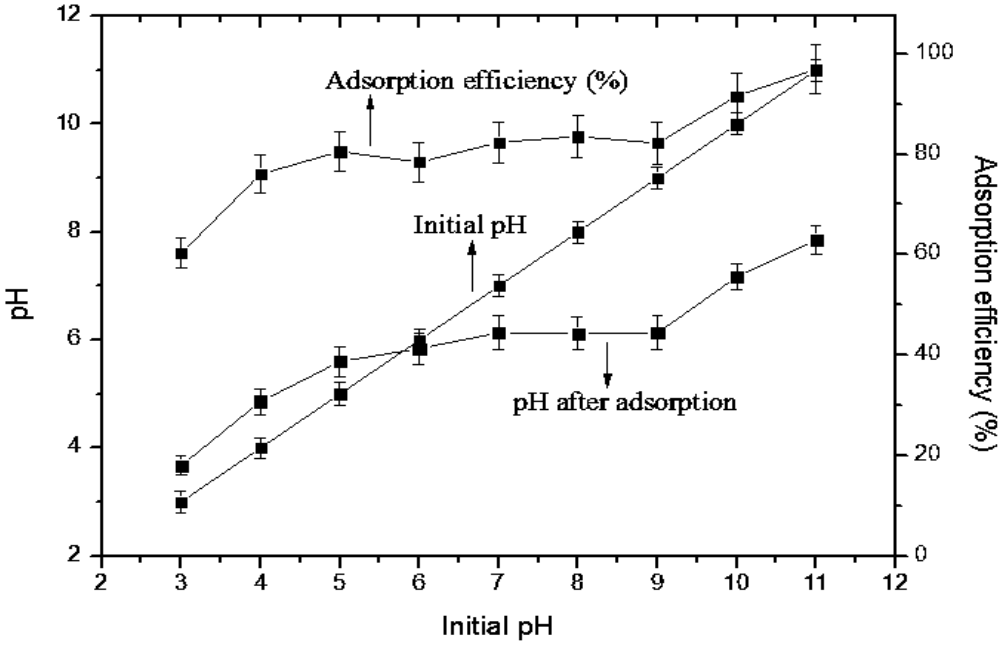

Fig. S9 Variations of initial pH and its influence in adsorption efficiency during adsorption